Available online at www.sciencedirect.com

ScienceDirect

Geochimica et Cosmochimica Acta 206 (2017) 112–136

Geochimica et Cosmochimica Acta

www.elsevier.com/locate/gca

The thermal decomposition of fine-grained micrometeorites, observations from mid-IR spectroscopy

Martin David Suttle [a,b,*], Matthew J. Genge [a,b], Luigi Folco [c], Sara S. Russell [b]

[a] Imperial College London, South Kensington, London SW72AZ, UK
[b] The Natural History Museum, Cromwell Rd, London SW7 5BD, UK
[c] Dipartimento di Scienze della Terra, Università di Pisa, 56126 Pisa, Italy

Received 29 September 2016; accepted in revised form 1 March 2017; available online 9 March 2017

Abstract

We analysed 44 fine-grained and scoriaceous micrometeorites. A bulk mid-IR spectrum (8–13 μm) for each grain was collected and the entire micrometeorite population classified into 5 spectral groups, based on the positions of their absorption bands. Corresponding carbonaceous Raman spectra, textural observations from SEM-BSE and bulk geochemical data via EMPA were collected to aid in the interpretation of mid-IR spectra. The 5 spectral groups identified correspond to progressive thermal decomposition. Unheated hydrated chondritic matrix, composed predominantly of phyllosilicates, exhibit smooth, asymmetric spectra with a peak at ~10 μm. Thermal decomposition of sheet silicates evolves through dehydration, dehydroxylation, annealing and finally by the onset of partial melting. Both CI-like and CM-like micrometeorites are shown to pass through the same decomposition stages and produce similar mid-IR spectra. Using known temperature thresholds for each decomposition stage it is possible to assign a peak temperature range to a given micrometeorite. Since the temperature thresholds for decomposition reactions are defined by the phyllosilicate species and the cation composition and that these variables are markedly different between CM and CI classes, atmospheric entry should bias the dust flux to favour the survival of CI-like grains, whilst preferentially melting most CM-like dust. However, this hypothesis is inconsistent with empirical observations and instead requires that the source ratio of CI:CM dust is heavily skewed in favour of CM material. In addition, a small population of anomalous grains are identified whose carbonaceous and petrographic characteristics suggest in-space heating and dehydroxylation have occurred. These grains may therefore represent regolith micrometeorites derived from the surface of C-type asteroids. Since the spectroscopic signatures of dehydroxylates are distinctive, i.e. characterised by a reflectance peak at 9.0–9.5 μm, and since the surfaces of C-type asteroids are expected to be heated via impact gardening, we suggest that future spectroscopic investigations should attempt to identify dehydroxylate signatures in the reflectance spectra of young carbonaceous asteroid families.

Keywords: Micrometeorite; Atmospheric entry; Mid-IR; Phyllosilicate; Dehydration

1. INTRODUCTION

Micrometeorites (MMs) are submillimetre dust grains which sample local solar system small bodies (Genge et al., 2008). This dust is liberated from parent bodies by impacts and collisional disruption (Nesvorný et al., 2003; Flynn et al., 2009), spontaneous disruption (Nesvorný et al., 2010), sublimation (Schulz et al., 2004; Yang et al., 2009)

* Corresponding author at: Imperial College London, South Kensington, London SW72AZ, UK.
E-mail addresses: mds10@ic.ac.uk (M.D. Suttle), m.genge@ic.ac.uk (M.J. Genge), luigi.folco@unipi.it (L. Folco), sara.russell@nhm.ac.uk (S.S. Russell).

http://dx.doi.org/10.1016/j.gca.2017.03.002
0016-7037/

and mantle shedding events (Schulz et al., 2015) creating a near continuous flux of material (Peucker-Ehrenbrink, 1996; Prasad et al., 2013). Dust grains spiral into the inner solar system in <1 Ma due to Poynting-Robertson drag (Poynting, 1904; Gonczi and Froeschlé, 1982) and are either captured by terrestrial planets or are consumed by the Sun (Nesvorný et al., 2006; Vokrouhlický et al., 2008). Micrometeorites dominate the dust flux, with 20,000–60,000 tons of material arriving on Earth each year (Love and Brownlee, 1993; Peucker-Ehrenbrink, 1996; Zolensky et al., 2006). Consequently, MMs represent a significant resource in planetary science, providing "sample returns" from the most primitive geological remnants of the early solar system. Based on observations of micrometeoroid trails using radar to reconstruct entry speeds (Janches et al., 2000) and through numerical modelling of atmospheric entry, which suggest a low-inclination, low-eccentricity source region (Love and Brownlee, 1991), the majority of MMs which survive entry most likely originate from the asteroid belt (Carrillo-Sánchez et al., 2015). However, a small fraction of MMs, found in Antarctic snow, are derived from cometary sources (Dobrică et al., 2012; Imae, 2012; Noguchi et al., 2015).

Petrological observations of over 5500 MMs collected at the South Pole Water Well suggest that up to 75% of the MM flux is friable material (Taylor et al., 2012). These fine-grained micrometeorites (FgMMs) can be subclassified into C1, C2 and C3 types based on the analysis of their microtextures, observed under back scatter electron (BSE) imaging as outlined in Genge et al. (2008). C1 particles present with homogenous, extensively hydrated matrix, and may contain magnetite crystallites while C2 grains are less aqueously altered and preserve a heterogeneous matrix containing anhydrous grains and chondrule fragments (Genge et al., 2005; van Ginneken et al., 2012). C3 FgMMs are anhydrous and highly porous, these grains are rare and not the focus of the present study. Multiple analyses, including petrologic (Kurat et al., 1994; Genge et al., 2005), geochemical (Steele, 1992; van Ginneken et al., 2012), isotopic (Engrand et al., 1999; Alexander et al., 2002; Suavet et al., 2010), textural (Genge et al., 1997) and organic matter analysis (Suzuki et al., 2010; Dobrică et al., 2011) have concluded that C1 and C2 FgMMs demonstrate close genetic affinities to hydrated, CI and CM carbonaceous chondrites. Given that chondrite specimens are relatively rare, while FgMMs are abundant (Maurette et al., 1991) with collections now amounting into the thousands of individual grains, MMs are important resources revealing the diversity among aqueously altered chondritic materials and potentially sample many more unique and unrepresented parent asteroids than their meteorite counterparts (Nesvorný et al., 2006; Gounelle et al., 2009). Both C1 and C2 populations of FgMMs are composed of phyllosilicates, either serpentine and/or saponite (Genge et al., 2001), which are observable under TEM and in XRD studies (Nakamura et al., 2001; Nozaki et al., 2006). Extraterrestrial phyllosilicates tend to be rich in Mg and Fe when compared to terrestrial phyllosilicates and typically present as clusters of short misorientated stacks (Noguchi et al., 2002) interspersed with hydrated, fibrous and radiating submicron tochilinite. Rare carbonates and anhydrous silicates, commonly forsterite and enstatite (Kurat et al., 1994; Genge et al., 1997) are also reported.

During atmospheric entry MMs experience rapid deceleration and subsequently flash heating (Love and Brownlee, 1991). The vast majority of grains, approximately 90% (Taylor et al., 1998) are completely destroyed, evapourating into the atmosphere; of the surviving material a high proportion are melted and quench crystallized forming cosmic spherules (CS) (Brownlee et al., 1997). A small fraction survive entry as unmelted grains whose peak temperatures may exceed 1000 °C (Love and Brownlee, 1991; Nozaki et al., 2006), under these conditions thermal reprocessing will significantly alter their pre-atmospheric mineralogy. Resolving parent body signatures from atmospheric overprinting is a major challenge in MM study. During entry phyllosilicates dehydrate, forming dehydroxylates (Genge et al., 2001; Nakamura et al., 2001). Simultaneously, inner igneous rims, resulting from thermal gradients (Genge, 2006) and outer spinel-magnetite rims resulting from the preferential concentration of Fe and loss of volatile phases, form on particle exteriors (Greshake et al., 1998; Toppani and Libourel, 2003). The decomposition of sulphides, organic matter and carbonates releases gas which form vesicles (Taylor et al., 2011). Several geochemical metrics, such as an increasing Fe/Si and Mn/Si ratio are commonly used as evidence of evapourative loss during heating (Genge, 2006). The petrographic thermal decomposition of MMs is therefore well-studied, however, the mid-IR spectroscopic signatures of MMs are relatively under studied.

Although several publications have demonstrated the utility of IR spectroscopy to the analysis of hydrated CM and CI carbonaceous chondrites (Sandford, 1984; Salisbury et al., 1991; Miyamoto and Zolensky, 1994; Beck et al., 2014), corresponding work on MMs is relatively rare. Exceptions include Osawa et al. (2001) a transmission study and Suzuki et al. (2010) a combined transmission-reflection study. However, both these studies focused on low-wavelength (~2.5–5.0 μm) features, primarily -OH and C-H stretching modes in organic molecules. By contrast, this study collects non-destructive reflectance spectra, focuses on the spectroscopy of the silicate fingerprint region (8-13 μm) and the evolution of inorganic minerals during entry heating.

Silicate minerals show spectral features in the 8–13 μm region associated with Si–O stretching vibrations in silica tetrahedra (Kieffer, 1979). Paired Christiansen features and Reststrahlen bands dominate this region. The Christiansen feature is a reflectance minimum appearing at ~8.5 μm for silicate minerals and occurs when the index of refraction for the medium light is travelling through, and the index of refraction of the mineral are equal (Prost, 1973). While Reststrahlen bands are mirror-like reflectance peaks which are associated with vibrational bands. Both Reststrahlen bands and the Christiansen feature are related to the composition of the sample (Salisbury, 1993). However, the Reststrahlen bands decrease in spectral contrast with decreasing grain size and increasing sample porosity; a consequence of volume scattering effects (Salisbury and Wald, 1992), this results

in a smooth indistinct but high intensity absorption band and a loss of compositional information. The fine-grained, high porosity regolith on many C-type and Trojan asteroid surfaces suffer from this problem (Vernazza et al., 2012; Hargrove et al., 2015). Despite the difficulties associated with resolving compositional information on small-body surfaces, the 8-13 μm region is of particular interest to planetary science as this spectral range is both observable from Earth, via ground-based and air-borne telescopes (Herter et al., 2012) and collected from space, via instruments such as the Spitzer Space Telescope (Houck et al., 2004) and the future James Webb Telescope (Gardner et al., 2006). As a result, a significant and increasing number of mid-IR spectra exist for asteroids (Landsman et al., 2016) and comets (Harker et al., 2010).

Laboratory studies on natural and analogue samples provide important ground-truth experiments for comparison with data collected from space telescopes. The analysis of carbonaceous chondrites by Beck et al. (2010, 2014) demonstrated that hydrated CM chondrites most closely resemble a single phyllosilicate mineral, saponite. Since the modal mineralogy of CM chondrites are dominated by phyllosilicate phases (~75 vol%), predominately Mg-rich serpentine and Fe-rich cronsteditite (Howard et al., 2009, 2011) it is unsurprising that CM spectra resemble terrestrial phyllosilicates. However, it is unusual that saponite spectral signatures, not serpentine, are a best match for CM chondrites, since serpentine is the dominant phyllosilicate in CM chondrites (Howard et al., 2009, 2011). This phenomena is attributed to either the low crystallinity of chondritic serpentines, or the effect of Fe/Mg cation substitution replacing the more typical Al/Si ions found in terrestrial phyllosilicates, thereby leading to a broadening of the absorption peaks (Beck et al., 2014). Previous mid-IR analysis of extraterrestrial dust has predominantly focused on the organic components held within primitive ultra-carbonaceous MMs and interplanetary dust particles (IDPs). Combined multi-element analysis has demonstrated a convincing spectral relationship between some primitive laboratory samples and cometary materials, notably Hale-Bopp (Brunetto et al., 2011; Dartois et al., 2013).

This study aims to characterise the thermal decomposition of FgMMs in the mid-IR, and pair spectroscopic observations against carbonaceous Raman data, bulk geochemical data and microtextural evidence. The evolution of micrometeoroids by flash heating during atmospheric entry is critical to resolve since this process significantly alters the precursor cosmic mineralogy. Furthermore, heated MMs may prove useful analogues for interpreting the heated surfaces of C-type asteroids (Nakamura, 2005; Ostrowski et al., 2010; Zolensky et al., 2016), currently considered the parent bodies of hydrated chondritic materials (Hartmann et al., 1987; Fornasier et al., 2016).

2. METHODS

2.1. Samples and preparation

Micrometeorites from the Transantarctic Mountain (TAM, $n = 8$), Cap Prudhomme (CP94, $n = 36$) and Larkman Nunatak collections (LK06, $n > 50$) were analysed in this study. Cap Prudhomme MMs were recovered by melting and filtering blue ice during the 1994 field expedition (Maurette et al., 1991). The TAM particles were recovered from exposed rock traps in Victoria Land on the Transantarctic mountains at Frontier Mountain and Miller Butte (Rochette et al., 2008; Suavet et al., 2009) and Larkman Nunatak MMs were recovered from dry, unconsolidated moraine deposits sandwiched between a blue-ice and drift snow deposits at Larkman Nunatak in the Grosvenor Mountains (Suttle et al., 2015).

The Larkman Nunatak MMs preserve only completely melted CS and partially melted scoriaceous micrometeorites (ScMMs), while the TAM and CP94 collections contain a full suite of petrologic types including abundant unmelted FgMMs. The Larkman CS were included in this study to provide examples of complete melting but are not the focus of our analysis; instead, we concentrate on the early stage heating and thermal decomposition of hydrated chondritic material.

The TAM particles used in this study are large, ranging from ~600 to >1500 μm (Suavet et al., 2009) and the Cap Prudhomme grains are small, typically below 150 μm. This contrast in grain sizes reflects differences in the length of collection between the two sites. In the TAM collection MMs accumulate by direct infall into rock traps (exposed weathering cracks) over long timescales (up to 1 Ma) (Suavet et al., 2009). Conversely, the Cap Prudhomme MMs are ice-stored, accumulate primarily by aeolian processes on the icesheet surface before being buried and sample the cosmic dust flux over the recent past (~50 Ka) (Maurette et al., 1994). This size disparity may result in differences in the composition, petrology and genetic affinities of the two MM populations since different parent bodies dominate the dust flux at difference size ranges (Tomeoka et al., 2003; Zolensky et al., 2006). The anhydrous CV, CO and ordinary chondritic material is more common among coarse size ranges (>300 μm) (van Ginneken et al., 2012) while hydrated CM and CI material dominates the smaller (<100 μm) size fractions (Flynn et al., 2009; Cordier and Folco, 2014). We included samples from both collections in order to better understand the MM flux and to determine whether anhydrous and hydrated parent bodies could be easily distinguished.

The degree of terrestrial weathering experienced by individual MMs can be summarised using the bimodal scheme outlined in van Ginneken et al. (2016). Numbers between 0 and 3 reflect the loss of primary material (0 being a pristine grain and 3 representing a grain with >60% loss), while letters A–C describe the degree of encrustation on the particle surface (A being no encrustation and C being a complete surface covering). Cap Prudhomme MMs exhibit weathering grades of 1-2A, the lack of encrustation on particle rims attests to the absence of abundant fluids in contact with the particle surface for significant periods of time (van Ginneken et al., 2016). Conversely, the TAM particles show more extensive weathering alteration, with weathering grades of 2-3B-C. Encrustation of jarosite and replacement of internal extraterrestrial mineralogy by weathering products is common (Suavet et al., 2009; van Ginneken et al.,

2016). Terrestrial weathering is unfortunate since it obscures the pre-atmospheric mineralogy and hinders petrographic analysis, for this reason only particles exhibiting the least terrestrial weathering effects from each MM collection were selected.

Micrometeorites had previously been washed, sieved and picked under optical microscope (particle exteriors were analysed in the case of the TAM particles). The grains were then embedded in resin, sectioned, polished and analysed under SEM. Each particle's extraterrestrial origin had previously been confirmed on the basis of chondritic elemental ratios for major and minor elements and distinctive textural features as outlined in Genge et al. (2008). A detailed account of sample preparation and processing can be found in Suavet et al. (2009) for the TAM collection and Genge et al. (1997) for the Cap Prudhomme collection. A suite of 8 carbonaceous chondrites were acquired as research loans from the Natural History Museum (NHM), London and included CM, CI and C2 ungrouped (Tagish Lake and Bells) meteorites. The choice of chondrites was determined by the availability of samples held in the museum's collections. These meteorites act as reference materials owing to their close affinities to hydrated FgMMs. A full list of the samples included in this study and their respective sources are shown in Table 1.

2.2. Experimental

This study collected mid-IR spectra, bulk compositions and carbonaceous Raman spectra for each MM. The following techniques provided both a petrographic and organic matter perspective and are well-suited to the analysis of small, thermally altered and geochemically complex samples.

Spectroscopic data were collected at Diamond Lightsource UK, using the spectroscopy and support lab 91. A ThermoFisher Scientific 6700 Nicolet Continuμm FT-IR microscope spectrometer was used. This system was equipped with a 32x IR objective lens, a KBr beamsplitter and a MCT-A detector (cooled with liquid nitrogen), providing an optimised setup for the measurement of mid-IR spectra. Spectra were collected in percentage reflectance mode. Each spectrum combined 120 integrated scans with a 4 cm^{-1} spectral sampling resolution. A reference background spectrum, collected upon a clean, polished gold standard (and resampled every hour), was subtracted from the raw data. Data were collected in air and standard corrections applied for atmospheric suppression using the in-house OMNIC software. It was not deemed necessary to perform analyses under vacuum since the silicate fingerprint region (the main focus of the present study) is not affected by molecular vibrations from air.

A global mid-IR spectrum was obtained for the small Cap Prudhomme and Larkman Nunatak MMs micrometeorites by altering the rectangular aperture on microscope to fit the size of the micrometeorite being analysed. Apertures of 50 μm × 50 μm were typical, covering the centre of the particle whilst avoiding the epoxy resin holding the grains. For the TAM micrometeorites several spectra were collected, ensuring that the entire exposed surface area of the particle was analysed. These spectra were then averaged to give a global spectrum. For the carbonaceous chondrite samples, spectra were collected using a 100 × 100 μm grid placed randomly within a meteorite's matrix.

Raw spectra were processed by clipping, reducing the spectral range from the total observed (~3.0–14.5 μm) to the range of interest (8–13 μm). Because the spectral profiles were flat, baseline processing was not necessary. In addition, since the size of the aperture varied between samples the percent reflectance values varied in magnitude; this was resolved by scaling the reflectance values of all spectra between 0 and 1 (thereby generating arbitrary reflectance units). This process allowed spectra from different samples to be compared. In all samples the Christiansen minimum equalled 0 and the maximum peak in the Reststrahlen bands equalled 1. In the case of the TAM particles several spectra were then averaged to generate a bulk spectrum.

Raman spectra were collected using a Reinshaw inVia Raman microscope. A 473 nm green Ar^{+} laser focused through a 50x objective lens provided a ~6 μm diameter interaction area. Care was taken to ensure an extremely low laser power (<80 μW) in accordance with standard analytical protocol for analysis of highly disordered carbonaceous phases (Bonal et al., 2006; Busemann et al., 2007); this prevented the graphitisation of organic matter (Kagi et al., 1994). Successive measurements over the same region of CM2 Cold Bokkeveld, were performed to ensure sample evolution did not occur during analysis. Raw Raman spectra were processed by fitting a 6th order polynomial baseline and exponentially smoothing the subtracted spectrum, following a similar methodology as Caro et al. (2008). The carbonaceous 'G' and 'D' bands in the processed spectra were then fitted against a conventional 2-part Lorentz and Breit-Wigner-Fano (LBWF) model. The goodness of fit between the model and the processed Raman spectra was evaluated using the residual sum of squares (RSS) statistic, which calculates the total deviation between the model and empirical data. RSS values greater than 2.5 were arbitrarily determined "bad fits" and the peak parameters rejected. For the remaining spectra, the peak parameters from several (typically > 10) individual spectra were averaged to give a representative value for each sample and the standard error of the mean ($\sigma\bar{x}$) calculated. In this study we focus on peak height ratio, commonly referred to as R_1, and calculated as $R_1 = I_D/I_G$ where I_x represents the peak intensity. This metric is known to accurately follow peak temperatures reached during sample heating (Rahl et al., 2005; Bonal et al., 2006) whilst also being the parameter with the least degree of analytical uncertainty.

Geochemical data were collected at the NHM in the Imaging and analysis centre. A Zeiss EVO LS15 analytical SEM with energy dispersive spectroscopy was employed for initial sample characterisation and collection of BSE images. Electron microprobe analyses (EMPA), recording major and minor element compositions were collected using the Cameca SX100 equipped with wave dispersive spectroscopy (WDS). San Carlos olivine, basaltic glasses and Kakanui augite mineral standards were used for calibration. During acquisition acceleration voltages of 20 kV,

Table 1
Micrometeorites studied in this work and their sources. A solid black circle indicates data were collected, an open circle represents missing data.

No.	Specimen	Type	Mid-IR (8-13μm)	Raman R_1	EMPA	Source
1	CP94-050-052	C2 - FgMM	G1	●	●	Cap Prudhomme
2	CP94-050-160	C2 - FgMM	G1	●	●	Cap Prudhomme
3	TAM-15.11	C1 - FgMM	G2	○	●	Transantarctic Mountains
4	TAM-18C-12	C1 - FgMM	G2	●	●	Transantarctic Mountains
5	TAM-4-27	C2 - FgMM	G2	●	○	Transantarctic Mountains
6	TAM-19B-17	C2 - FgMM	G2	●	●	Transantarctic Mountains
7	TAM-19-7	ScMM	G2	●	●	Transantarctic Mountains
8	CP94-050-074	C1 - FgMM	G3	●	●	Cap Prudhomme
9	CP94-050-139	C1 - FgMM	G3	●	●	Cap Prudhomme
10	CP94-050-140	C1 - FgMM	G3	●	●	Cap Prudhomme
11	CP94-050-067	C2 - FgMM	G3	●	●	Cap Prudhomme
12	CP94-050-115	C2 - FgMM	G3	●	●	Cap Prudhomme
13	TAM-4-16	C2 - FgMM	G3	○	○	Transantarctic Mountains
14	CP94-050-054	C1 - FgMM	G4	●	●	Cap Prudhomme
15	CP94-050-183	C1 - FgMM	G4	●	●	Cap Prudhomme
16	CP94-050-163	C1 - FgMM	G4	●	●	Cap Prudhomme
17	CP94-050-169	C1 - FgMM	G4	●	●	Cap Prudhomme
18	CP94-050-176	C1 - FgMM	G4	●	●	Cap Prudhomme
19	CP94-050-269	C1 - FgMM	G4	●	●	Cap Prudhomme
20	CP94-050-063	C2 - FgMM	G4	●	●	Cap Prudhomme
21	CP94-050-129	C2 - FgMM	G4	●	●	Cap Prudhomme
22	CP94-050-130	C2 - FgMM	G4	●	●	Cap Prudhomme
23	TAM-19B-18	C2 - FgMM	G4	●	●	Transantarctic Mountains
24	CP94-050-159	C2 - FgMM	G4	●	●	Cap Prudhomme
25	TAM-5-30	C2 - FgMM	G4	○	●	Transantarctic Mountains
26	CP94-050-071	ScMM	G4	●	●	Cap Prudhomme
27	CP94-050-109	ScMM	G4	●	●	Cap Prudhomme
28	CP94-050-064	C1 - FgMM	G5	●	●	Cap Prudhomme
29	CP94-050-180	C1 - FgMM	G5	●	●	Cap Prudhomme
30	CP94-050-060	C2 - FgMM	G5	●	●	Cap Prudhomme
31	CP94-050-080	C2 - FgMM	G5	●	●	Cap Prudhomme
32	CP94-050-096	C2 - FgMM	G5	●	●	Cap Prudhomme
33	CP94-050-113	C2 - FgMM	G5	●	●	Cap Prudhomme
34	CP94-050-123	C2 - FgMM	G5	●	●	Cap Prudhomme
35	CP94-050-127	C2 - FgMM	G5	●	●	Cap Prudhomme
36	CP94-050-136	C2 - FgMM	G5	●	●	Cap Prudhomme
37	CP94-050-142	C2 - FgMM	G5	●	●	Cap Prudhomme
38	CP94-050-152	C2 - FgMM	G5	●	●	Cap Prudhomme
39	CP94-050-153	C2 - FgMM	G5	●	●	Cap Prudhomme
40	CP94-050-166	C2 - FgMM	G5	●	●	Cap Prudhomme
41	CP94-050-170	C2 - FgMM	G5	●	●	Cap Prudhomme
42	CP94-050-048	ScMM	G5	●	●	Cap Prudhomme
43	CP94-050-079	ScMM	G5	●	●	Cap Prudhomme
44	CP94-050-090	ScMM	G5	●	●	Cap Prudhomme
45	Tagish Lake	C2 ungrouped	G1	●	●	NHM - P11243
46	Bells	C2 ungrouped	G1	○	○	NHM - P9530
47	Ivuna	CI1	G1	●	●	NHM - P16384
48	AHLA81002	CM2	G1	●	●	NHM - P10918
49	Murray	CM2	G1	●	●	NHM - P20501
50	Mighei	CM2	G1	●	●	NHM - P20492
51	Jbilet Winselwan	CM2	G1	●	●	NHM - P18927
52	Cold Bokkeveld	CM2	G1	●	●	NHM - P20501
	>50 Cosmic spherules	CS	G5	○	○	Larkman Nunatak

beam currents of 10nA and a focused beam spot of <4 μm diameter were maintained. Standard Cameca matrix corrections were applied.

The bulk geochemical composition for each sample (is shown in Table 2 and) was determined by averaging multiple (typically $n > 7$) randomly located spot analyses from within the fine-grained matrix. By their nature matrix analyses are multiphase since the interaction volume unequally excites a mixed submicron mineral assemblage and the resulting X-rays produce a biased sample of the elemental composition (Rinaldi and Llovet, 2015). Hydrated minerals further lower totals since hydrogen is not detectable by EMPA. Consequently, low analytical totals are expected from chondritic and hydrated matrix (Noguchi et al., 2002; Rubin et al., 2007). However, totals below 70%, most likely due to sample porosity, were rejected. Although

Table 2
The prevalence of petrologic textures within micrometeorite samples. A particle's matrix is defined as vesicular where several roughly circular vesicles are present and this is different from the abundant scoriaceous texture composed of abundant small and interconnected vesicles.

	Group 1	Group 2	Group 3	Group 4	Group 5
No. of MMs	2	5	6	14	17
C2 FgMMs	100%	40%	50%	43%	70%
C1 FgMMs	0%	40%	50%	43%	12%
ScMMs	0%	20%	0%	14%	18%
Dehydration cracks	0%	80%	50%	100%	100%
Magnetite rims	0%	100%	67%	86%	88%
Igneous rims	0%	80%	50%	72%	41%
Vesicular matrix	0%	40%	0%	72%	59%

detection limits for trace elements in a single WDS analysis are typically on the order of 200–400 ppm, equivalent to 0.02–0.04 wt%, by acquiring and averaging multiple analyses, several of which record the presence of an element at or near the detection limit, it is possible to derive an average concentration for a sample below the analytical detection limit which remains meaningful; these values should however be treated with caution.

3. RESULTS

3.1. Mid-IR spectroscopy of micrometeorites and carbonaceous chondrites

All samples produced silicate fingerprints with a Christiansen minimum and Reststrahlen bands, transparency features were not observed over the wavelength range studied. The position of reflectance peaks are therefore diagnostic of their component minerals. Samples were separated into 5 spectral groups based on reflectance peak positions, examples are shown in Fig. 1. Carbonaceous chondrites (CM, CI and C2 ungrouped) have spectra with smooth, asymmetrical profiles dominated by a single peak whose maxima lies around 10 μm. In C2 Bells, CI1 Ivuna, C2 Tagish Lake and CM2 Cold Bokkeveld the primary peak lies at 9.89 μm, 9.95 μm, 10.01 μm and 10.07 μm respectively. In the remaining samples, all CM2 chondrites, peaks are broader and the maxima are shifted to higher wavelengths, around 10.5 μm. A small subordinate peak at 11.5 μm is present in most of the chondrites and is most clearly resolved in C2 Tagish Lake and CM2 Jbilet Winselwan. We designate this spectral profile group 1. Two FgMMs have group 1 spectra, CP94-050-052 and CP94-050-160. The spectra of CP94-050-160, whose peak position is 10.2 μm and which lacks a peak at 11.5 μm most closely resembles CM2 Cold Bokkeveld. The spectra of CP94-050-052 carries a low signal-to-noise ratio, its peak maxima appears to be at 10.2 μm and therefore similar to the other group 1 FgMM. The remaining 42 FgMMs are split into 4 spectral groups.

Group 2 spectra are represented by only 5 members all of which are from the TAM collection. Group 2 spectra are characterised by a relatively sharp and dominant peak at 9.0–9.5 μm and a profile which downslopes towards higher wavelengths. A series of smaller peaks at 10.01 μm, 10.89 μm, 11.3 μm and 11.7 μm can be resolved in TAM-19-7 and TAM-4-27 while the remaining group members have smooth, indistinct spectra expect for the presence of the aforementioned primary peak.

Group 3 spectra are represented by 6 FgMMs, predominantly from the Cap Prudhomme collection. This group demonstrates similarities to group 2 spectra; containing a well-defined Christiansen minimum and sharp rise to a peak at 9.0–9.5 μm (as seen in group 2), whilst also containing several additional peaks, most notably a peak at 10.8 μm and smaller features at ~10 μm and 11.4–11.8 μm. Spectra from this group tend to have a higher signal-to-noise ratio and this may indicate a small grain size, at the limit of the wavelength of impinging light and consequently the effect of volume scattering.their overall shape resembles the carbonaceous chondrite profile, whilst also containing a prominent peak at 9.0–9.5 μm and several additional peaks, most notably a peak at 10.8 μm and smaller features at ~10 μm and 11.4–11.8 μm. Spectra from this group tend to have a higher signal-to-noise ratio and this may indicate a small grain size, at the limit of the wavelength of impinging light and consequently the effect of volume scattering.

Group 4 spectra include 12 FgMMs and 2 ScMMs. Group 4 spectra bear a close resemblance to group 3 spectra, their peak positions are nearly identical but the relative peak intensities differ. While the peak at 9.0–9.5 μm is present the dominant peak is at 11.5 μm, and this results in an upsloping or reddening spectral profile.

Group 5 objects are the most populous group and include 14 FgMM and 3 ScMMs; their spectra are remarkably consistent between samples and have a primary absorption band at 11.5 μm, this is shouldered by peaks at 10.4–10.8 μm and at 12.4 μm.

The 5 spectral groups can be generalised by extracting their reflectance values at three key wavelengths: 9.95 μm, 10.7 μm and 11.5 μm, these being the approximate positions of the primary absorption bands for groups 1, 3 and 4–5. This data is plotted in Fig. 2 as a scatter diagram (9.95 μm vs. 10.7 μm /11.5 μm). Each of the spectral groups (with the exception of a merged population of group 2 and 3 objects) occupies a distinct domain. The mid-IR spectra of the FgMM population can then be accurately described by a single trend line with a negative correlation, a 2nd order polynomial whose R^2 regression value is 0.9 was fitted to this data. As the 11.5 μm peak increases the 9.95 μm

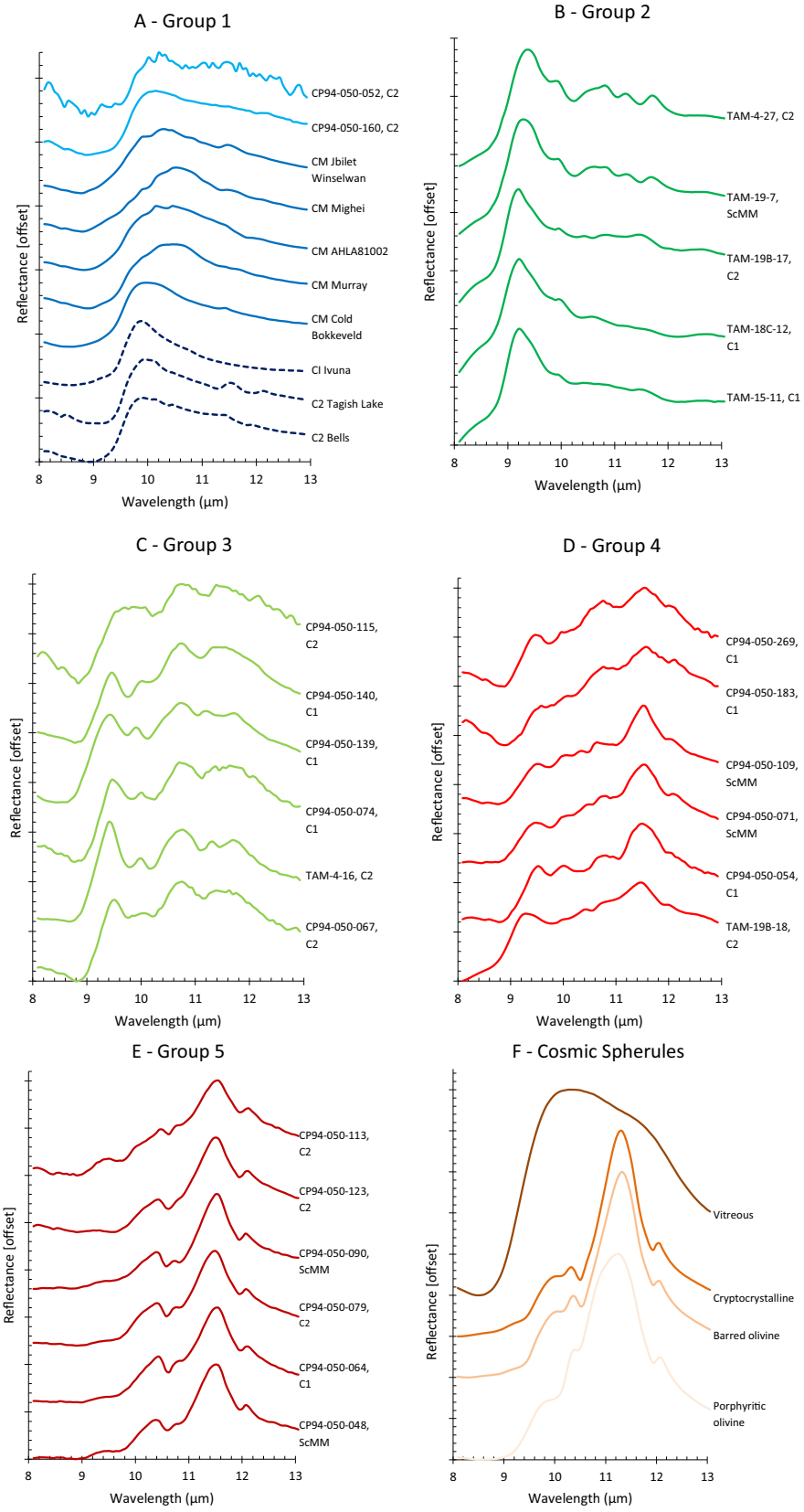

Fig. 1. Mid-IR spectra (8–13 μm) of selected carbonaceous chondrites and FgMMs. The MM population was separated into 5 spectral groups, on the basis of their reflectance peak positions, six plots (A–F) display the characteristic spectral profiles for each spectral group and example spectra of CS from Larkman Nunatak.

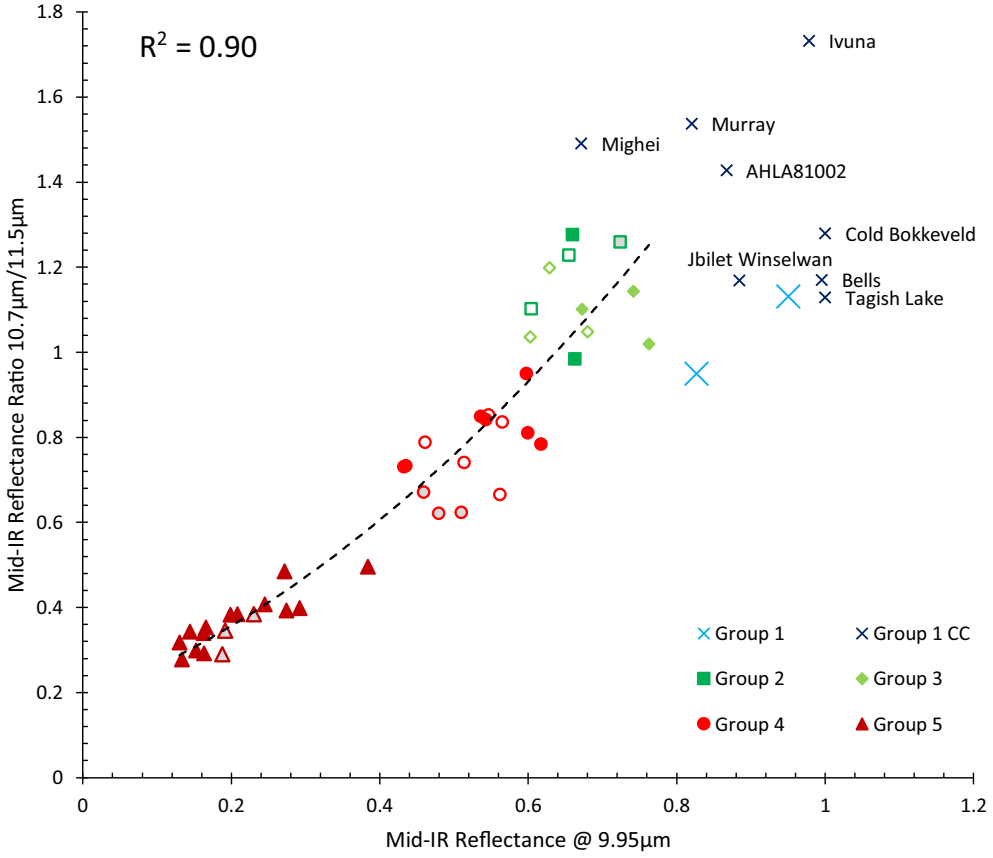

Fig. 2. Summary plot of mid-IR spectral groups 1–5. The x-axis plots reflectance values at 9.95 μm and the y-axis plots the ratio of reflectance values at 10.7 μm/11.5 μm. This plot illustrates the relationships between spectral groups and the carbonaceous chondrites. The entire FgMM population can be described by a single (polynomial) trend-line with a negative correlation and R^2 value of 0.9, illustrating that, although distinct, the spectral groups form a continuous set of related profiles, with group 5 objects being most similar to group 4 objects and group1-3 sharing similar characteristics. In this plot spectral group are represented by different colours and shapes: blue crosses for group 1 MMs, purple crosses for chondrites, dark green squares for group 2, light green diamonds for group 3, red circles for group 4 and dark red triangles for group 5. In addition, solid fill denote C2-FgMMs, open shapes denote C1-FgMMs and grey-infilled shapes are ScMMs. (For interpretation of the references to colour in this figure legend, the reader is referred to the web version of this article.)

decreases, the presence of peaks at 9.0–9.5 μm and at 10.7 μm are intermediate stages.

3.2. Petrography of fine-grained micrometeorites

This study analysed 44 MMs, BSE imaging allowed classification of this population into subtypes. Of the 38 FgMMs, 63% have C2 or CM-like textures while 37% showed C1 or CI1-like textures. For the remaining 6 particles it was not possible to determine their pre-atmospheric textures with confidence due to the presence of significant mesostasis, generated by the recrystallization of partial melts that formed during atmospheric entry. These grains are therefore classified as ScMMs. The classification of each MM as either C1, C2 or ScMM is shown in Table 1. In general C1 particles are more common among spectral groups 1–3 while C2 particles, although present in all spectral groups are more common among the groups 4 and 5.

Examples of C1 and C2 FgMMs and their internal microtextures are shown in Fig. 3. In C1 particles the matrix is compact, dense, homogenous and very fine-grained. Individual phyllosilicate crystals cannot normally be resolved. Magnetite is typically abundant and occurs as either platelets or framboids, both of which are present in CP94-050-140 (pictured, Fig. 3A). Close up images of the magnetite platelets demonstrate small vesicles and irregular crystal rims which may be surrounded by submicron halos of brighter matrix. Conversely, C2 particles by definition contain several different mineral phases in close proximity. The matrix phyllosilicates may vary significantly in chemical composition as determined (qualitatively) from variations in in their BSE Z values, this can be as micron-scale irregularities representing a fine-grained intermix of phyllosilicate species or as distinct clasts with sharp compositional and textural boundaries. The anhydrous silicates in C2 particles are generally small (<4 μm) and compositionally homogeneous.

The FgMM population demonstrates a range of petrographic features associated with entry heating including: igneous rims, magnetite rims, dehydration cracks, rounded vesicles and bright (high Z value) atomically heavy zones of matrix. The prevalence of these features in each spectral

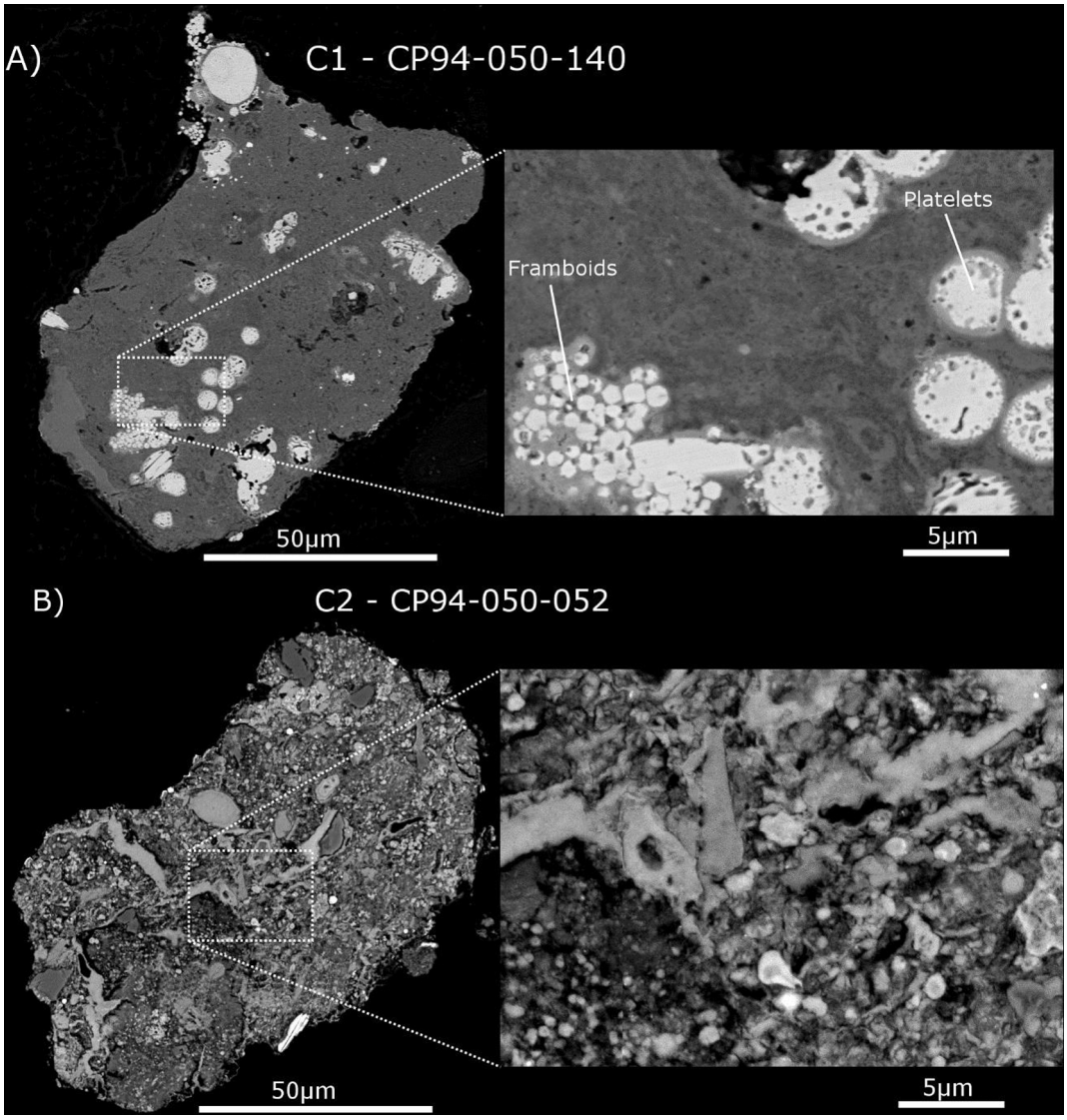

Fig. 3. BSE image panel illustrating examples of C1 (A) and C2 (B) FgMMs. C1 particles are characterised by a compact, homogenous, fine-grained matrix with interspersed magnetite framboids and/or magnetite platelets. While C2-FgMMs contain a heterogeneous matrix, with a variable Mg/Fe ratio in phyllosilicates (this is reflected in the mottled greyscale texture under BSE). Anhydrous silicates, carbonates, sulphides are common. For each grain a magnified rectangle is shown.

group are shown in Table 3 and examples of FgMMs from each mid-IR spectral group are shown in Fig. 4.

3.3. Mid-IR spectral groups and matrix geochemistry

The bulk matrix geochemistry for each grain is presented in Table 3 and plotted in Fig. 5 as a ternary diagram, using renormalized concentrations of their major elements (Mg, Fe and Si + Al). The stoichiometric compositions of saponite and serpentine, dependent on the Si + Al content, are marked as dashed lines. As is consistent with chondritic material, the MM population demonstrates a variable Fe concentration (between 20 and 80 normalised wt%) while their Mg, Si and Al concentrations are more restricted. The majority of the MM population plots within the carbonaceous chondrite compositional field, marked by a grey shaded oval, however, some FgMMs extend outside this range, to higher Fe concentrations. In general C1 FgMMs present with Si + Al enriched compositions, typically inbetween the serpentine and saponite stoichiometric bands while C2 FgMMs are Si + Al poor and Fe-rich.

The bulk matrix geochemistry of FgMMs was compared against their mid-IR spectral groups. Since this study explores the thermal decomposition of FgMMs during atmospheric entry, attention is drawn to elements with different volatilities; these are shown in Fig. 6. The behaviour of refractory (Al), moderately refractory (Mg), moderately volatile (Mn) and highly volatile (Cl) are presented.

No trend exists between mid-IR spectral groups and the concentration of refractory Al ($R^2 = 0.07$); for all groups

Table 3
Geochemical data for all samples studied. EMPA data are shown in weight percent, average values which fall below the detection limits of the Cameca SX100 are highlighted in grey. ND = no data collected.

	Specimen	Type	Group	N = (EMPA)	Na	Mg	Al	Si	P	S	Cl	K	Ca	Ti	Cr	Mn	Fe	Co	Ni	Cu	Zn	O	Total
1	CP94-050-052	C2 - FgMM	G1	12	0.17	2.86	0.73	7.39	0.16	0.49	0.36	0.03	1.17	0.09	0.44	0.18	36.14	0.00	0.33	1.05	1.79	23.90	77.29
2	CP94-050-160	C2 - FgMM	G1	7	0.24	4.45	1.82	12.45	0.08	1.16	0.28	0.08	0.74	0.08	0.31	0.07	24.81	0.07	1.11	0.55	2.18	29.28	79.76
3	TAM-15.11	C1 - FgMM	G2	11	0.28	2.53	3.04	17.70	0.11	2.62	ND	1.29	0.16	0.08	0.43	0.07	20.43	0.00	0.09	0.02	0.01	35.17	84.01
4	TAM-18C-12	C1 - FgMM	G2	18	0.30	1.24	1.16	15.67	0.18	4.98	ND	1.59	0.18	0.10	0.63	0.03	25.91	0.00	0.21	0.02	0.03	35.75	87.99
5	TAM-4-27	C2 - FgMM	G2	0	ND	ND	ND	ND	ND	ND	ND	ND	ND	ND	ND	ND	ND	ND	ND	ND	ND	ND	ND
6	TAM-19B-17	C2 - FgMM	G2	25	0.18	3.04	1.68	17.56	0.16	2.72	ND	0.61	0.14	0.09	0.39	0.08	26.67	0.00	0.14	0.01	0.02	35.97	89.45
7	TAM-19-7	ScMM	G2	19	0.70	5.88	1.96	19.67	0.01	3.35	ND	1.16	0.15	0.08	0.45	0.09	18.31	0.00	0.22	0.04	0.00	39.20	91.25
8	CP94-050-074	C1 - FgMM	G3	9	0.32	12.63	1.64	21.83	0.16	0.46	0.09	0.15	0.16	0.09	0.44	0.05	13.80	0.00	0.42	0.30	0.71	40.34	93.58
9	CP94-050-139	C1 - FgMM	G3	7	0.13	9.64	1.32	16.69	0.22	0.33	0.32	0.08	0.22	0.06	0.58	0.08	14.54	0.00	0.34	0.35	0.89	32.37	78.18
10	CP94-050-140	C1 - FgMM	G3	7	0.22	16.16	1.56	21.83	0.12	0.28	0.10	0.08	0.17	0.06	0.33	0.12	10.34	0.00	0.15	0.13	0.43	40.99	93.06
11	CP94-050-067	C2 - FgMM	G3	15	0.33	9.80	1.17	17.26	0.04	0.40	0.14	0.06	0.21	0.09	0.40	0.14	21.64	0.00	0.15	0.73	1.06	34.99	88.60
12	CP94-050-115	C2 - FgMM	G3	6	0.36	6.00	1.18	13.18	0.30	0.47	0.49	0.09	0.53	0.09	0.50	0.10	25.76	0.00	0.07	0.77	1.11	29.65	80.66
13	TAM-4-16	C2 - FgMM	G3	0	ND	ND	ND	ND	ND	ND	ND	ND	ND	ND	ND	ND	ND	ND	ND	ND	ND	ND	ND
14	CP94-050-054	C1 - FgMM	G4	13	0.47	10.17	1.46	17.52	0.10	0.20	0.27	0.13	0.25	0.07	0.36	0.17	16.26	0.00	0.22	0.46	0.67	33.95	82.74
15	CP94-050-183	C1 - FgMM	G4	7	0.12	8.27	1.25	15.07	0.20	0.47	0.30	0.07	0.31	0.08	0.37	0.13	23.30	0.00	0.13	0.74	1.30	32.35	84.46
16	CP94-050-163	C1 - FgMM	G4	7	0.41	12.18	1.66	19.00	0.10	0.44	0.20	0.11	0.71	0.08	0.42	0.20	15.27	0.01	0.27	0.28	0.58	37.35	89.28
17	CP94-050-169	C1 - FgMM	G4	7	0.22	13.40	1.37	18.23	0.18	0.44	0.12	0.06	0.20	0.83	0.41	0.14	17.15	0.02	0.47	0.15	0.74	37.93	92.08
18	CP94-050-176	C1 - FgMM	G4	8	0.21	13.65	1.71	19.85	0.09	0.42	0.12	0.08	0.25	0.05	0.42	0.10	14.27	0.02	0.77	0.10	0.60	38.80	91.53
19	CP94-050-269	C1 - FgMM	G4	6	0.28	12.64	1.53	18.50	0.44	0.50	0.23	0.16	0.33	0.08	0.41	0.15	16.69	0.00	0.20	0.48	0.86	37.79	91.26
20	CP94-050-063	C2 - FgMM	G4	7	0.15	5.15	0.83	6.81	0.22	0.46	0.35	0.03	0.44	0.06	0.29	0.17	37.39	0.01	0.48	0.60	1.74	24.74	79.91
21	CP94-050-129	C2 - FgMM	G4	3	0.14	7.22	1.01	12.38	0.41	0.38	0.32	0.06	0.47	0.07	0.37	0.15	23.53	0.00	0.16	1.35	1.05	28.75	77.83
22	CP94-050-130	C2 - FgMM	G4	7	0.28	9.70	1.18	16.17	0.15	0.34	0.29	0.07	0.45	0.08	0.39	0.18	19.29	0.00	0.20	0.28	0.83	32.98	82.84
23	TAM-19B-18	C2 - FgMM	G4	20	0.23	7.65	1.66	14.77	0.08	1.94	ND	0.30	0.17	0.06	0.33	0.17	32.03	0.01	0.27	0.01	0.02	36.06	95.75
24	CP94-050-159	C2 - FgMM	G4	3	0.59	11.10	1.27	17.05	0.19	0.33	0.31	0.16	0.48	0.08	0.38	0.15	16.27	0.00	0.13	0.15	0.41	34.14	83.18
25	TAM-5-30	C2 - FgMM	G4	22	0.08	11.53	2.03	18.28	0.10	0.81	ND	0.29	2.03	0.10	0.30	0.13	19.96	0.02	0.47	0.01	0.01	38.57	94.73
26	CP94-050-071	ScMM	G4	6	0.48	8.14	1.69	16.86	0.24	0.52	0.18	0.14	0.79	0.08	0.30	0.17	20.78	0.00	0.22	0.81	0.94	34.36	86.72
27	CP94-050-109	ScMM	G4	9	0.61	12.94	1.31	19.62	0.10	0.59	0.10	0.12	0.59	0.06	0.44	0.22	16.88	0.01	0.23	0.08	0.61	38.91	93.42
28	CP94-050-064	C1 - FgMM	G5	11	0.22	10.56	1.48	15.32	0.15	0.69	0.06	0.09	0.51	0.06	0.55	0.22	30.55	0.04	0.79	0.23	0.51	36.77	98.81
29	CP94-050-180	C1 - FgMM	G5	7	0.28	13.85	1.60	18.64	0.13	1.04	0.16	0.07	0.18	0.07	0.36	0.12	16.63	0.04	0.98	0.32	0.50	39.19	94.17
30	CP94-050-060	C2 - FgMM	G5	7	0.19	9.76	1.40	15.79	0.17	0.36	0.10	0.09	0.16	0.07	0.24	0.19	30.24	0.00	0.19	0.15	0.49	35.65	95.23
31	CP94-050-080	C2 - FgMM	G5	7	0.08	10.56	0.51	13.80	0.22	0.40	0.13	0.01	0.97	0.05	0.28	0.19	30.90	0.01	0.30	0.16	0.38	33.73	92.69
32	CP94-050-096	C2 - FgMM	G5	13	0.18	9.67	1.58	13.65	0.12	0.55	0.12	0.07	0.32	0.05	0.27	0.20	32.12	0.03	0.57	0.22	0.43	34.26	94.42
33	CP94-050-113	C2 - FgMM	G5	7	0.45	8.77	2.00	15.35	0.28	0.73	0.20	0.21	0.57	0.07	0.30	0.15	21.61	0.04	1.20	0.16	0.97	33.97	87.04
34	CP94-050-123	C2 - FgMM	G5	6	0.15	11.07	1.02	14.98	0.22	0.46	0.13	0.05	0.16	0.09	0.27	0.21	29.22	0.00	0.32	0.16	0.48	35.23	94.23
35	CP94-050-127	C2 - FgMM	G5	7	0.28	12.22	1.42	17.19	0.23	0.63	0.07	0.12	0.36	0.08	0.46	0.23	23.28	0.02	0.41	0.18	0.47	37.67	95.31
36	CP94-050-136	C2 - FgMM	G5	7	0.28	10.94	1.62	16.15	0.09	0.71	0.04	0.10	0.15	0.08	0.36	0.25	27.14	0.02	0.45	0.05	0.43	36.73	95.61
37	CP94-050-142	C2 - FgMM	G5	7	0.14	10.14	1.26	15.09	0.21	0.46	0.08	0.05	0.16	0.07	0.40	0.20	29.25	0.01	0.27	0.11	0.60	34.99	93.49
38	CP94-050-152	C2 - FgMM	G5	7	0.33	14.95	1.41	18.44	0.04	0.30	0.06	0.08	0.11	0.06	0.22	0.21	21.46	0.00	0.15	0.03	0.32	39.27	97.46
39	CP94-050-153	C2 - FgMM	G5	7	0.38	11.35	1.43	15.06	0.21	0.40	0.15	0.09	0.64	0.06	0.44	0.26	24.35	0.03	0.68	0.17	0.71	34.89	91.30
40	CP94-050-166	C2 - FgMM	G5	9	0.22	13.02	1.37	16.65	0.11	0.40	0.08	0.07	0.33	0.05	0.34	0.20	26.11	0.02	0.32	0.08	0.48	37.69	97.55
41	CP94-050-170	C2 - FgMM	G5	12	0.22	13.18	1.40	15.75	0.10	0.48	0.10	0.05	0.45	0.07	0.26	0.22	26.22	0.01	0.35	0.16	0.40	36.97	96.40
42	CP94-050-048	ScMM	G5	8	0.31	14.14	1.02	18.73	0.17	0.43	0.08	0.06	1.72	0.09	0.43	0.21	18.33	0.03	0.46	0.08	0.31	39.03	95.64
43	CP94-050-079	ScMM	G5	10	0.31	12.66	1.20	15.88	0.12	0.51	0.09	0.09	0.22	0.06	0.29	0.21	25.91	0.01	0.31	0.22	0.38	36.53	95.02
44	CP94-050-090	ScMM	G5	7	0.31	14.77	1.25	18.85	0.21	1.05	0.06	0.11	0.42	0.07	0.44	0.23	17.98	0.04	0.84	0.14	0.39	40.30	97.46
45	Tagish Lake	C2 ung	G1	1	0.24	10.58	0.91	9.87	0.07	1.25	0.10	0.06	1.09	0.02	0.12	0.22	19.88	0.00	0.533	0.00	0.01	27.484	72.43
46	Bells	C2 ung	G1	0	ND	ND	ND	ND	ND	ND	ND	ND	ND	ND	ND	ND	ND	ND	ND	ND	ND	ND	ND
47	Ivuna	CI1	G1	34	0.28	12.21	1.13	14.78	0.16	2.83	0.15	0.03	0.43	0.04	0.33	0.14	15.28	0.07	1.49	0.01	0.05	35.64	85.05
48	AHLA81002	CM2	G1	13	0.40	10.61	0.95	13.73	0.05	2.15	0.24	0.06	0.20	0.05	0.31	0.19	19.03	0.11	1.82	0.01	0.06	33.22	83.20
49	Murray	CM2	G1	22	0.09	8.50	1.40	12.94	0.08	0.91	0.08	0.02	0.41	0.05	0.28	0.17	26.57	0.07	1.50	0.01	0.03	31.50	84.61
50	Mighei	CM2	G1	31	0.42	9.25	0.95	11.92	0.22	2.23	0.36	0.04	0.74	0.04	0.41	0.19	20.28	0.12	2.20	0.01	0.04	31.32	80.76
51	Jbilet Winselwan	CM2	G1	17	0.60	8.00	1.26	12.15	0.10	1.24	0.26	0.15	1.15	0.05	0.29	0.19	29.58	0.08	1.80	0.01	0.03	32.14	89.08
52	Cold Bokkeveld	CM2	G1	10	0.44	10.32	1.21	14.03	0.07	2.69	0.04	0.05	0.60	0.06	0.29	0.20	25.65	0.07	1.55	0.01	0.03	36.42	93.74

abundances vary between 0.5 and 2.0 wt%, within the expected chondritic range, this lack of correlation is true for other refractory elements, including Ca and Ti. However, for moderately refractory Mg a weak geochemical trend exists ($R^2 = 0.3$), in groups 1–3 Mg concentrations span a wide range of values, from 2.8–16.1 wt%, this range decreases to 5.2–13.6 wt% for spectral group 4 objects and is limited further to 8.7–14.9 wt% among group 5. Although the range becomes restricted, generally the average Mg concentration increases from groups 1–3 through group 4–5 objects, as a result a weak negative correlation is observed. For the moderately volatile elements such as Mn, a strong negative correlation is seen ($R^2 = 0.68$). Mn concentrations in group 1–3 range from 0.05 wt% (near the limit of detection of 0.03 wt%) up to 0.18 wt%, however, this range is reduced and the average concentration increases in both group 4 and subsequently group 5. The behaviour of highly volatile Cl, also demonstrates a moderate positive correlation ($R^2 = 0.35$); groups 1–3 occupy the largest concentration range from 0.1–0.5 wt%, this decreases for group 4 to a more limited range between 0.09 and 0.35 wt% and decreases further for group 5 from 0.03 wt% (the detection limit) to 0.2 wt%. The above observations can be summarised by stating that MMs in spectral groups 4 and 5 are progressively enriched in moderately refractory elements and correspondingly depleted in volatile components, while the reverse is true for MMs in spectral groups 1–3.

3.4. Mid-IR spectral groups and comparisons with Carbonaceous Raman peak parameters

Raman peak parameter data is shown in Table 4, example Raman spectra are shown in Fig. 7 and the relationship between Raman R_1 values and mid-IR spectral group is shown in Fig. 8. Collectively the FgMM and chondrite population display a moderate negative correlation ($R^2 = 0.60$) between R_1 peak height ratios and mid-IR spectral groups, in general as the 10.7 μm/11.5 μm ratio decreases so the R_1 ratio increases. Carbonaceous chondrite R_1 values range from 0.4 to 0.6, while the group 1 FgMMs plot between 0.45 and 0.7. The majority of group 2 and 3 FgMMs extend to slightly higher R_1 values, between 0.5 and 0.7. However, in spectral groups 4 and 5 the MM populations show progressively higher R_1 values reaching up to $R_1 = 1.2$. A small collection of 6 FgMMs in spectral group 5, show anomalous R_1 values, which do not fit the trend described above. The anomalous grains are predominantly C2 FgMMs.

4. DISCUSSION

4.1. The thermal decomposition of micrometeorites

The selection of carbonaceous chondrites used in this study provides a range of analogue materials with different post-accretion histories, different bulk compositions and phyllosilicate complements. As a result, although hydrated

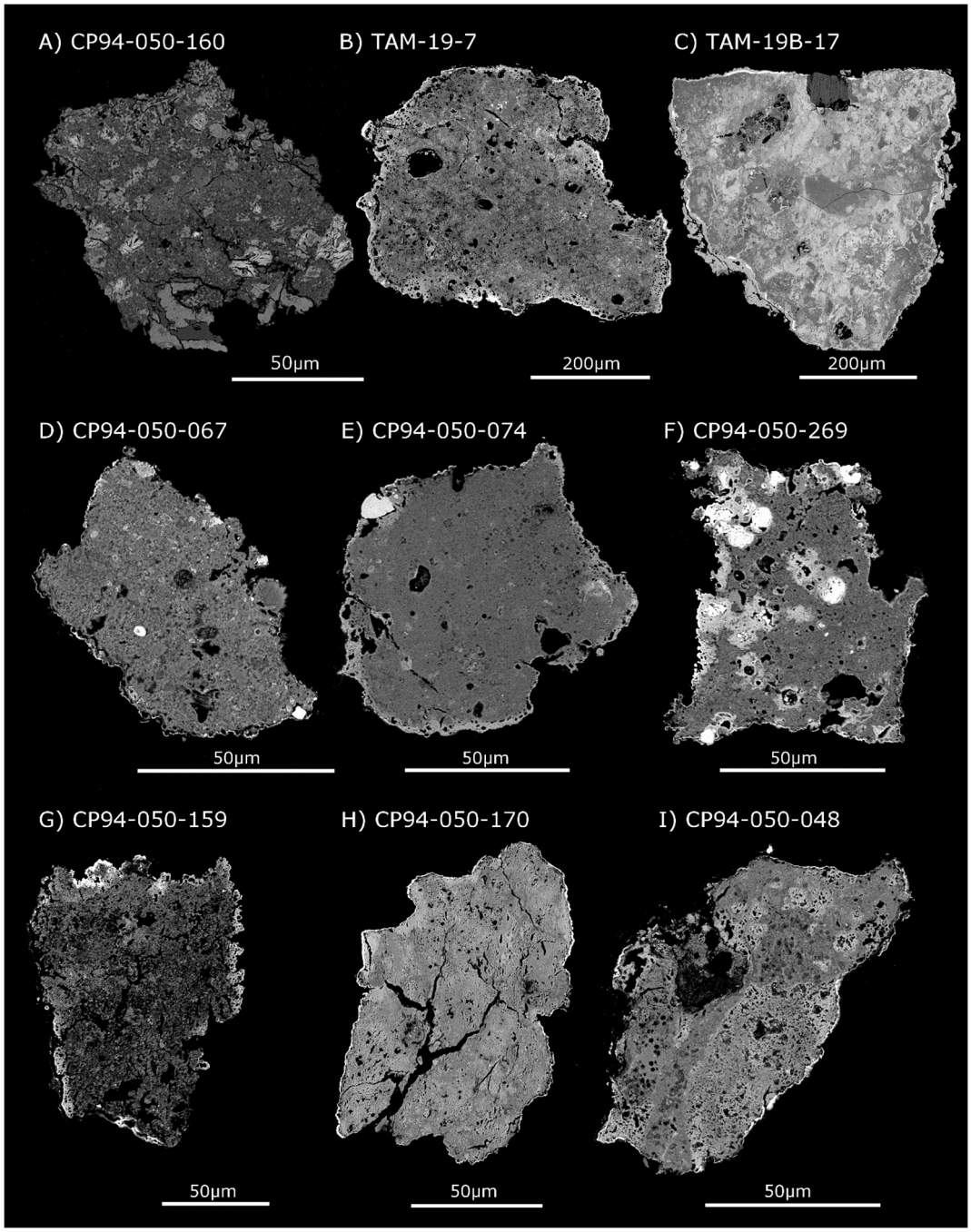

Fig. 4. BSE image panel illustrating examples of FgMMs from each of the mid-IR spectral groups defined in the result section. Particle A is a group 1 FgMM (with the remaining grain [CP94-050-052] shown in Fig. 3). While grains B and C are from group 2, D and E from group 3, F and G from group 4 and H and I from group 5. A range of petrologic features (characteristic of entry heating alteration) are present including dehydration cracks, most clearly shown in (H) CP94-050-170, igneous rims clearly shown in both (B) TAM-19-7 and CP94-050-074, Fe-enriched (atomically heavy, bright) altered and vesicular matrix shown in (F) CP94-050-269 and magnetite rims shown in (C) TAM-19B-17.

chondrites all exhibit similar, unheated phyllosilicate spectra, significant variation in their spectral profiles can be discerned, as demonstrated in Figs. 1 and 2. The diversity of samples represented provides a suite for comparison and therefore, aids the interpretation of the heated MM population.

Two significant geochemical processes may affect the shape of the 10 μm phyllosilicate peak; the degree of aqueous alteration (Rubin et al., 2007) and the degree of parent body metamorphism (Tonui et al., 2003, 2014; Nakato et al., 2013). The range of chondrites presented in this study span moderately altered samples such as CM Murray and CM Mighei (Rubin et al., 2007; Howard et al., 2009) to highly altered CM chondrites such as AHLA 81002 (Hanowski and Brearley, 2001) and the intensely altered, CI chondrite, Ivuna (Tonui et al., 2003). A range of peak

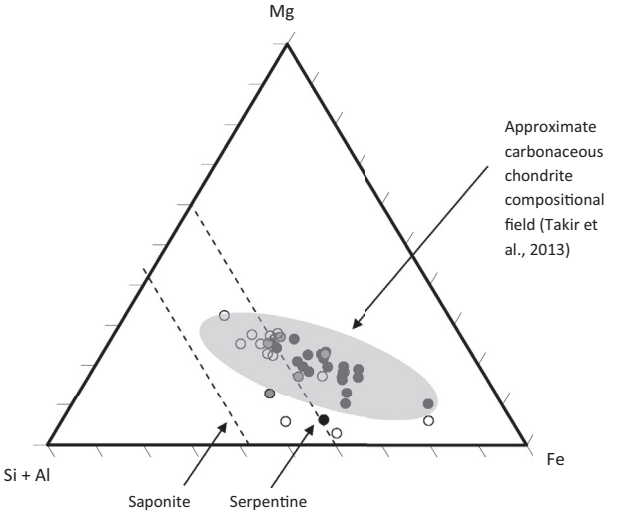

Fig. 5. Ternary diagram illustrating the normalised (Mg, Fe and Si + Al in wt%) bulk matrix compositions for the MM population (40 of 44). The stoichiometric elemental ratios for saponite and serpentine phyllosilicates and the compositional field for chondritic matrix are shown for comparison. The majority of the FgMM sit within the chondritic compositional range. However, some MMs are Fe-enriched, representing atmospheric entry heating effects and some particles are Mg deficient, representing the effects of terrestrial weathering. Solid black circles represent C2-FgMMs, open circles C1-FgMMs and grey-filled circles ScMMs. (See above-mentioned references for further information.)

metamorphic temperatures are also represented; the majority of CM chondrites did not experience parent body temperatures >300 °C (Nakamura, 2005; Busemann et al., 2007). Meteorites such as AHLA81002, Murray and Mighei are examples of these low-temperature CM chondrites (Busemann et al., 2007). Conversely, a growing collection of meteorites show evidence of higher grade thermal metamorphism (Nakamura, 2005; Nakato et al., 2013). In this collection, Jbilet Winselwan (Zolensky et al., 2016) and Cold Bokkeveld (Quirico et al., 2014) are examples of heated (>300 °C, <700 °C) CM chondrites.

Since phyllosilicates dominate the mineralogy of hydrated chondritic matrix, the behaviour of these minerals during thermal decomposition will control the spectral profiles of heated FgMMs. Experimental heating of phyllosilicate standards by Che and Glotch (2012), heating of CM/CI chondrites (Nozaki et al., 2006; Nakato et al., 2008) and extensive previous SEM study of FgMM decomposition products allows the thermal evolution of phyllosilicates to be understood (Genge et al., 1997; Genge, 2007). Phyllosilicates undergo contraction on heating, owing to evaporation of absorbed inter-layer water causing silicate sheets to contract; this is referred to as dehydration (Drits and McCarty, 2007). With continued heating structural water is lost and sheet silicates collapse forming an amorphous, or partially crystalline phase described as a dehydroxylate (Wang et al., 2002; Zhang et al., 2010). In phyllosilicates structural water is present as M–OH bonds in octahedral layers, where the M represents a metal cation and is typically Al^{3+} in terrestrial phyllosilicates but may be substituted abundantly by Mg^{2+} and Fe^{2+} in chondritic clays (Che and Glotch, 2012). If heating continues dehydroxylates will anneal and recrystallize as olivine or pyroxene. These recrystallized anhydrous silicates can be distinguished from primary olivine due to their characteristic low crystallinity and hyperfine grain size (Greshake et al., 1998; Tonui et al., 2003).

Dehydration reactions are the first stage of phyllosilicate thermal decomposition. In FgMMs contraction of sheet silicates leads to dehydration cracks forming in the matrix (Toppani et al., 2001; Genge, 2008) this is observable in BSE images. However, no spectroscopic change accompanies this loss of water, as demonstrated by the spectra of Jbilet Winselwan (Fig. 1A) which appears similar to other CM chondrites despite a near complete dehydration of matrix phases (Zolensky et al., 2016). Consequently, dehydrated MMs will be indistinguishable from unheated and low-grade (<300 °C) thermally metamorphosed CM/CI chondrites in the mid-IR. Since inter-layer water is not structurally bonded to the silicate framework water vibrations should not be expected in the 8-13 μm silicate fingerprint region, instead hydration evidence is observable in the 3 μm NIR spectral domain (Feierberg et al., 1985; Campins et al., 2010). Given the strong resemblance between the group 1 FgMMs (CP94-050-052 and CP94-050-160) and chondritic spectra these grains cannot have experienced significant thermal reprocessing and must preserve either intact or partially dehydrated phyllosilicates. Since high Raman R_1 values are associated with higher peak temperatures, and since CP94-050-052 and CP94-050-160 demonstrate low R_1 values (0.7 and 0.6 respectively), within (or just outside) the range of the CI/CM chondrite population, this suggests these MMs have not experienced significant heating above that endured by the CM2 chondrite population (<300 °C) (Busemann et al., 2007). Furthermore, the retention of highly volatile Cl at concentrations above 0.26 wt% and only minimal enrichment of moderately volatile Mn also confirm atmospheric entry temperatures were low (<600 °C) (Nozaki et al., 2006). In addition CP94-050-160 preserves large, fibrous tochilinite masses, this mineral is highly unstable and decomposes above 245 °C (Nazarov et al., 2009), and as a result its retention provides an upper bounds to peak entry temperatures. The matrix in CP94-050-052 retains a strongly heterogeneous texture with abundant and clearly resolvable grains, approximately 1–5 μm in size, as shown in Fig. 3; this matrix texture is distinct from the more "welded" texture of heated C2-FgMMs, where thermal reprocessing has led to the decomposition of volatile phases, recrystallization and partial melting, overprinting the pristine chondritic texture.

The most prominent feature observed in most FgMM spectra is the distinctive 9.0–9.5 μm peak present in group 2, 3 and 4. This peak is attributed to dehydroxylated phyllosilicates. Once structural water is lost, a sudden change in the mid-IR spectra is observed, characterised by a shift in the primary absorption band from 9.5–10 μm in intact phyllosilicates to 9.0–9.5 μm for dehydroxylates. This behaviour is present in clay minerals (but not mica sheet silicates) and was identified in the present study after examining the thermal decomposition pathways of the

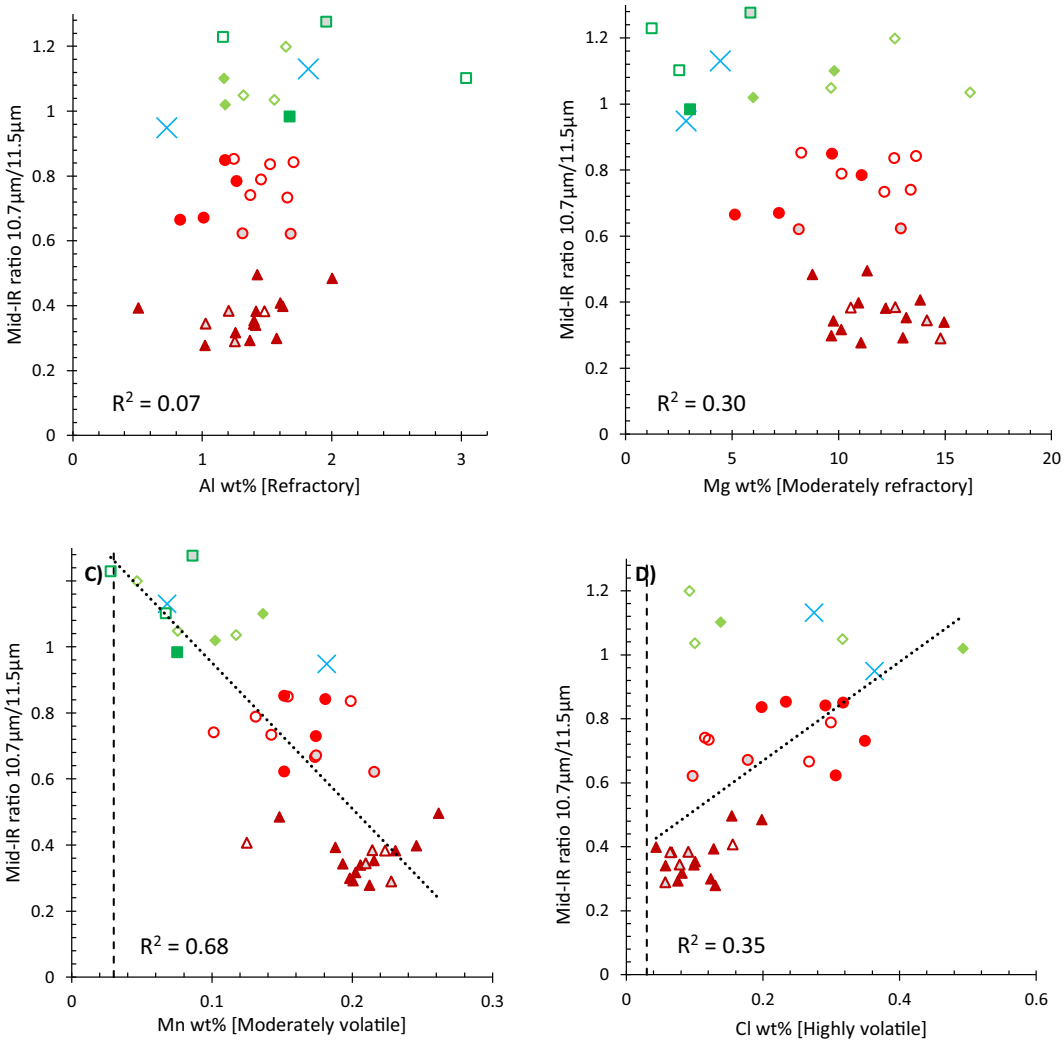

Fig. 6. Comparisons between mid-IR spectral groups and bulk matrix geochemistry, with focus drawn to the behaviour of (A) refractory [Al], (B) moderately refractory [Mg], (C) moderately volatile [Mn] and (D) highly volatile [Cl]. In this plot spectral group are represented by different colours and shapes: blue crosses for group 1 MMs, purple crosses for chondrites, dark green squares for group 2, light green diamonds for group 3, red circles for group 4 and dark red triangles for group 5. In addition, solid fill denote C2-FgMMs, open shapes denote C1-FgMMs and grey-infilled shapes are ScMMs.

experimentally heated phyllosilicate spectra shown in Che and Glotch (2012), this behaviour is highlighted in Fig. 9. Dehydroxylates are mineraloids with an indistinct chemical structure, however some SiO_4 tetrahedra and Si–O–M linkages are retained, reflecting the former layered structure (Wang et al., 2002; Madejová, 2003) and it is this amorphous network with intact Si–O bonds which is responsible for the ~9.0–9.5 µm spectral signature.

The mid-IR spectra of group 2 and 3 FgMMs are dominated by dehydroxylates, their peak positions are identical but the relative intensities of the two groups differ markedly. Group 2 objects most closely resemble saponite dehydroxylates, as shown in Che and Glotch (2012), while the group 3 spectra resemble amorphous silicates with an enstatite composition (Hallenbeck et al., 1998). This is due to the increased peak height at 10.7 µm and growth of smaller peaks at 11.5 µm and 12.2 µm. For group 3 particles, small quantities of micron-scale anhydrous enstatite crystallites may be present, having formed by annealing of the dehydroxylate phases. Group 2 spectra are only observed in the larger TAM particles while group 3 spectra are seen in both the TAM and Cap Prudhomme collections. Three of the TAM FgMMs in group 2 have smooth and featureless spectra (with the exception of the 9.0–9.5 µm peak). The presence of indistinct, broad and merged peaks reflects a lack of long range order and subsequently a low degree of crystallinity (Speck et al., 2011). These FgMMs have experienced extensive weathering, as determined by the complete encrustation of K and Na bearing jarosite, and partial replacement of their pre-atmospheric mineralogy with terrestrial weathering products. The atomic structure is therefore approaching an amorphous state and bears resemblance to the weathered vitreous CS reported in van Ginneken et al. (2016) that are altered to palagonite.

Table 4
Raman peak parameters for all samples studied, standard error of the mean values are denoted by σx.

No.	Specimen	Type	Mid-IR (8-13μm)	N = (Raman)	D-Position	D-Position (σx̄)	D-FWHM	D-FWHM (σx̄)	G-position	G-position (σx̄)	G-FWHM	G-FWHM (σx̄)	R1	R1 (σx̄)	Source
1	CP94-050-052	C2 - FgMM	G1	26	1369.7	1.7	122.5	4.6	1590.5	1.0	97.1	3.4	0.69	0.06	Cap Prudhomme
2	CP94-050-160	C2 - FgMM	G1	27	1372.2	0.9	124.1	2.5	1593.8	0.4	85.2	1.3	0.44	0.01	Cap Prudhomme
3	TAM-15.11	C1 - FgMM	G2	0	ND	ND	ND	ND	ND	ND	ND	ND	ND	ND	Transantarctic Mountains
4	TAM-18C-12	C1 - FgMM	G2	6	1371.0	1.4	114.9	5.3	1596.1	1.9	105.5	5.4	0.60	0.03	Transantarctic Mountains
5	TAM-4-27	C2 - FgMM	G2	4	1373.8	6.5	132.0	14.6	1587.3	4.1	111.2	10.1	0.74	0.08	Transantarctic Mountains
6	TAM-19B-17	C2 - FgMM	G2	5	1371.0	4.5	135.6	18.0	1595.2	1.4	94.3	2.9	0.67	0.06	Transantarctic Mountains
7	TAM-19-7	ScMM	G2	7	1369.4	2.1	108.4	10.8	1594.3	1.3	87.1	8.0	0.64	0.06	Transantarctic Mountains
8	CP94-050-074	C1 - FgMM	G3	16	1370.5	1.7	116.0	4.0	1592.5	1.1	101.2	2.4	0.61	0.05	Cap Prudhomme
9	CP94-050-139	C1 - FgMM	G3	14	1373.8	1.7	118.5	6.0	1587.6	1.4	99.8	3.3	0.60	0.05	Cap Prudhomme
10	CP94-050-140	C1 - FgMM	G3	23	1377.1	1.3	127.8	3.2	1591.0	0.5	113.0	1.2	0.45	0.01	Cap Prudhomme
11	CP94-050-067	C2 - FgMM	G3	17	1371.8	1.6	127.1	4.5	1592.1	0.5	102.7	2.2	0.53	0.02	Cap Prudhomme
12	CP94-050-115	C2 - FgMM	G3	20	1362.5	1.2	124.3	3.1	1589.8	0.5	100.5	2.6	0.62	0.03	Cap Prudhomme
13	TAM-4-16	C2 - FgMM	G3	0	ND	ND	ND	ND	ND	ND	ND	ND	ND	ND	Transantarctic Mountains
14	CP94-050-054	C1 - FgMM	G4	14	1371.3	1.7	114.2	6.1	1587.4	1.9	79.0	3.5	1.05	0.11	Cap Prudhomme
15	CP94-050-183	C1 - FgMM	G4	16	1367.1	1.2	130.8	3.9	1590.1	0.7	98.3	4.1	0.72	0.06	Cap Prudhomme
16	CP94-050-163	C1 - FgMM	G4	40	1366.9	1.2	125.5	3.1	1591.4	0.6	99.5	2.5	0.69	0.03	Cap Prudhomme
17	CP94-050-169	C1 - FgMM	G4	23	1371.8	0.9	130.0	2.1	1593.2	0.5	107.2	1.6	0.57	0.01	Cap Prudhomme
18	CP94-050-176	C1 - FgMM	G4	9	1368.4	1.3	122.5	5.3	1592.6	1.1	105.9	2.8	0.58	0.03	Cap Prudhomme
19	CP94-050-269	C1 - FgMM	G4	14	1367.3	1.7	124.4	3.4	1592.0	0.8	107.2	1.9	0.63	0.03	Cap Prudhomme
20	CP94-050-063	C2 - FgMM	G4	16	1359.8	1.1	120.8	3.7	1589.9	0.4	89.4	3.3	0.61	0.02	Cap Prudhomme
21	CP94-050-129	C2 - FgMM	G4	8	1367.9	3.5	122.6	11.2	1589.6	2.4	90.2	5.9	0.82	0.10	Cap Prudhomme
22	CP94-050-130	C2 - FgMM	G4	12	1370.8	2.2	117.8	5.8	1591.1	1.2	93.1	4.2	0.75	0.07	Cap Prudhomme
23	TAM-19B-18	C2 - FgMM	G4	8	1374.7	3.3	129.3	7.7	1594.6	1.4	99.6	2.3	0.74	0.11	Transantarctic Mountains
24	CP94-050-159	C2 - FgMM	G4	22	1365.8	1.0	125.9	4.5	1589.2	0.6	88.3	2.5	0.78	0.04	Cap Prudhomme
25	TAM-5-30	C2 - FgMM	G4	0	ND	ND	ND	ND	ND	ND	ND	ND	ND	ND	Transantarctic Mountains
26	CP94-050-071	ScMM	G4	0	ND	ND	ND	ND	ND	ND	ND	ND	ND	ND	Cap Prudhomme
27	CP94-050-109	ScMM	G4	17	1372.1	1.7	126.7	6.8	1589.9	1.8	92.4	5.3	0.85	0.09	Cap Prudhomme
28	CP94-050-064	C1 - FgMM	G5	3	1372.8	2.1	132.0	10.8	1593.3	1.7	101.4	6.3	0.63	0.07	Cap Prudhomme
29	CP94-050-180	C1 - FgMM	G5	12	1366.7	3.0	134.9	9.2	1588.7	2.2	87.3	4.8	0.89	0.12	Cap Prudhomme
30	CP94-050-060	C2 - FgMM	G5	2	1370.5	2.4	119.9	6.8	1592.2	0.4	105.8	0.8	0.53	0.05	Cap Prudhomme
31	CP94-050-080	C2 - FgMM	G5	14	1368.2	1.5	118.3	6.9	1593.0	1.7	77.2	3.2	1.02	0.08	Cap Prudhomme
32	CP94-050-096	C2 - FgMM	G5	11	1367.3	3.4	114.2	8.8	1590.8	1.2	102.7	6.8	0.62	0.05	Cap Prudhomme
33	CP94-050-113	C2 - FgMM	G5	18	1365.2	2.3	116.8	6.8	1591.1	0.9	84.2	4.0	0.89	0.08	Cap Prudhomme
34	CP94-050-123	C2 - FgMM	G5	5	1367.3	7.2	117.3	15.5	1595.0	2.5	81.3	3.9	1.18	0.32	Cap Prudhomme
35	CP94-050-127	C2 - FgMM	G5	18	1371.1	2.6	123.4	7.7	1591.0	1.0	103.7	4.0	0.52	0.04	Cap Prudhomme
36	CP94-050-136	C2 - FgMM	G5	17	1373.4	2.0	108.0	7.6	1587.0	0.6	111.6	3.1	0.41	0.04	Cap Prudhomme
37	CP94-050-142	C2 - FgMM	G5	16	1374.1	1.4	114.6	5.5	1587.4	0.9	115.5	2.5	0.41	0.02	Cap Prudhomme
38	CP94-050-152	C2 - FgMM	G5	14	1370.0	2.3	122.2	5.6	1592.0	2.2	100.4	5.6	0.86	0.10	Cap Prudhomme
39	CP94-050-153	C2 - FgMM	G5	17	1370.2	2.8	130.4	8.8	1590.3	1.3	97.3	3.9	0.69	0.06	Cap Prudhomme
40	CP94-050-166	C2 - FgMM	G5	8	1372.9	3.6	129.1	10.8	1585.1	2.3	90.3	7.9	1.05	0.13	Cap Prudhomme
41	CP94-050-170	C2 - FgMM	G5	19	1371.7	1.6	130.9	4.6	1590.3	1.4	99.0	3.7	0.87	0.06	Cap Prudhomme
42	CP94-050-048	ScMM	G5	16	1372.6	1.8	123.0	4.8	1588.4	2.1	103.0	4.3	0.85	0.08	Cap Prudhomme
43	CP94-050-079	ScMM	G5	24	1371.3	1.4	130.4	5.1	1591.1	2.0	97.7	5.1	0.89	0.09	Cap Prudhomme
44	CP94-050-090	ScMM	G5	23	1373.7	1.8	126.1	5.9	1590.4	1.2	107.7	2.9	0.71	0.05	Cap Prudhomme
45	Tagish Lake	C2 ungrouped	G1	11	1379.1	0.7	110.9	3.0	1592.5	0.6	88.4	2.2	0.42	0.03	NHM - P11243
46	Bells	C2 ungrouped	G1	11	1374.9	1.9	101.2	6.9	1589.3	0.9	90.5	3.9	0.51	0.05	NHM - P9530
47	Ivuna	CI1	G1	11	1374.3	0.9	98.4	2.8	1590.0	0.6	88.7	1.3	0.52	0.02	NHM - P16384
48	AHLA81002	CM2	G1	14	1370.3	1.1	105.2	3.5	1592.5	0.7	82.1	2.2	0.59	0.04	NHM - P10918
49	Murray	CM2	G1	9	1369.2	1.1	123.1	3.2	1593.3	0.8	92.9	1.7	0.55	0.03	NHM - P20501
50	Mighei	CM2	G1	7	1372.1	1.0	111.1	3.7	1593.0	0.3	87.8	2.3	0.59	0.03	NHM - P20492
51	Jbilet Winselwan	CM2	G1	21	1372.2	0.8	121.2	3.0	1594.6	0.3	85.0	1.4	0.51	0.02	NHM - P18927
52	Cold Bokkeveld	CM2	G1	11	1382.1	0.9	142.3	5.1	1591.9	0.6	97.4	1.4	0.44	0.01	NHM - P20501

However, the remaining 2 FgMMs in spectral group 2 (TAM-19-7 and TAM-4-27) are more crystalline, their reflectance peaks are relatively sharp and the positions suggest a partially crystalline dehydroxylate structure.

The average R_1 Raman parameters for both group 2 and 3 are not statistically different from either each other or CM/CI chondrites, spanning a restricted range from $R_1 = 0.4$–0.8, this suggests that both group 2 and 3 MMs have experienced similar modest thermal reprocessing. Although the group 2 TAM particles all show magnetite rims and most also support igneous rims, vesicles and dehydration cracks, their larger size ensures that while the rim may be significantly heated the particle core is capable of retaining an unheated (and pre-atmospheric) or only mildly reprocessed mineralogy (Genge and Grady, 2000). In addition the geochemical ranges for Mg and Mn in both groups are similar, suggesting that one group is not more heated that the other. Therefore, it is unlikely that the difference in spectral signatures relate to different peak temperatures. The disparity between these two dehydroxylate signatures is probably a product of either different species, or mixtures of species of phyllosilicate and may also be influenced by the action of increased terrestrial weathering experienced by the TAM particles. Since different parent bodies are expected to dominate the dust flux at different size ranges, and since group 2 is entirely composed of the larger TAM MMs it is likely that group 2 and group 3 represent different pre-atmospheric mineralogies; although in the present study it is not possible to characterise the phyllosilicate species. Since both groups have peak positions consistent with the spectra of dehydroxylated phyllosilicates, these groups must represent FgMMs which have experienced peak temperatures between 300–700 °C resulting in the loss of structural water and collapse of the sheet silicate structures.

Group 4 spectra also retain the 9.0–9.5 μm dehydroxylate peak, however, this population is spectrally distinct from group 2 and 3, instead showing a reddening slope (defined by increasing reflectance with increasing wavelength) and a dominant peak at 11.5 μm. This is the characteristic primary absorption band for olivine and is shouldered by smaller peaks at 10.7 μm and 12.2 μm. The appearance of anhydrous olivine and retention of the dehydroxylate peak implies the matrix is partially recrystallized. This requires annealing of the amorphous phases and suggests group 4 spectra have experienced higher peak temperatures, or longer duration heating than group 2 and 3 spectra. The average R_1 values for group 4 spectra are higher than group 2 and 3 (between 0.5 and 1.0). Additionally, increases in Mg and Mn and corresponding decreases in Cl when compared against group 2 and 3 FgMMs support the conclusion of higher peak temperatures in group 4. The onset of dehydroxylate recrystallization was empirically observed in hydrated chondrites at ~700 °C and therefore provides a minimum peak entry temperature

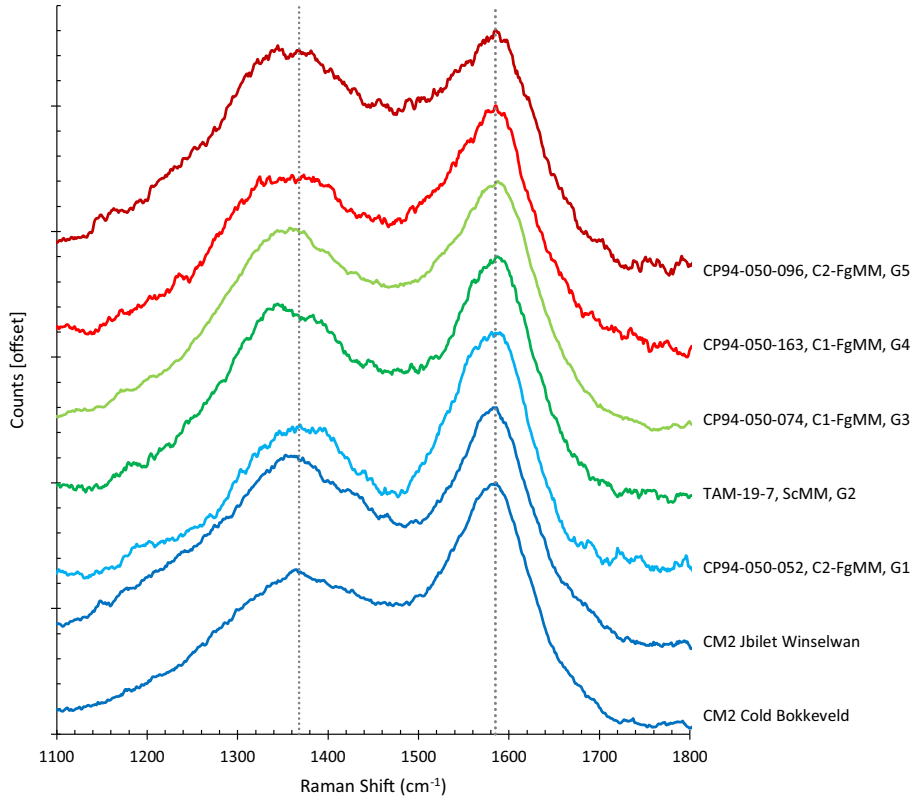

Fig. 7. Example Raman spectra from each (mid-IR) spectral group. Spectra have been processed by baseline removal and exponential smoothing and are offset by on the y-axis for clarity. The resulting profiles contain prominent carbonaceous D and G bands, located at approximately 1365 cm^{-1} and 1590 cm^{-1} Raman shift values respectively. These bands reflect the highly disordered carbonaceous phases present within hydrated chondritic matrix. Spectra are colour coordinated, corresponding to their mid-IR spectral class; purple for CM chondrites, blue for group 1 (FgMMs), dark green for group 2, light green for group 3, red for group 4 and dark red for group 5. (For interpretation of the references to colour in this figure legend, the reader is referred to the web version of this article.)

for these MMs (Akai, 1992; Nozaki et al., 2006; Nakato et al., 2008).

The mid-IR spectra of group 5 objects are spectroscopically identical to olivine (Koike et al., 2006), implying that dehydroxylates are absent and the entire matrix has experienced complete recrystallization, forming secondary anhydrous phases. The chemical composition of the matrix in these grains is consistent with a high degree of thermal reprocessing and supports the conclusion of high peak temperatures. Group 5 MMs are the most enriched in moderately refractory Mg and moderately volatile Mn whilst being significantly depleted in highly volatile Cl (for most micrometeorites this is near the detection limit of 0.03 wt %). This behaviour reflects the progressive evaporative loss of more volatile elements as peak temperatures rise (Genge, 2006). Group 5 samples have therefore experienced the highest peak entry temperatures. Despite significant entry reprocessing, many of these FgMMs retain a pseudomorphic matrix which resembles both the texture of hydrated chondrites and earlier stages of thermal decomposition. For example, CP94-050-170, shown in Fig. 4, preserves subparallel dehydration cracks. These cracks would have formed during atmospheric entry at lower peak temperatures as phyllosilicates decomposed, although this grain then experienced further heating and mineral phase changes, resulting in a recrystallized groundmass of fine-grained olivine, the dehydration cracks remain visible. Some C2 FgMMs also retain their diagnostic heterogeneous matrix texture, with sharp compositional boundaries between relict clasts as shown in CP94-050-060 in Fig. 10. The retention of relict fabric despite complete recrystallization confirms that olivine formation occurs by solid state annealing processes, essentially forming metamorphic olivine, as opposed to melting and subsequent cooling resulting in igneous olivine. The ability to distinguish relict clasts in a recrystallized groundmass demonstrates that little diffusion or homogenisation of chemical variations occurs. This is because recrystallization is rapid (<10 s) (Love and Brownlee, 1991) and kinetic effects prohibit the migration of elements over micron length scales by solid state diffusion (Grossman and Brearley, 2005). As peak temperatures increase above 700 °C, annealing will continue and the grains size and crystallinity of the MM matrix will increase and relict textures will eventually be entirely overprinted. At the onset of partial melting ScMMs form, this is typically attributed to temperatures above 1350 °C (Toppani

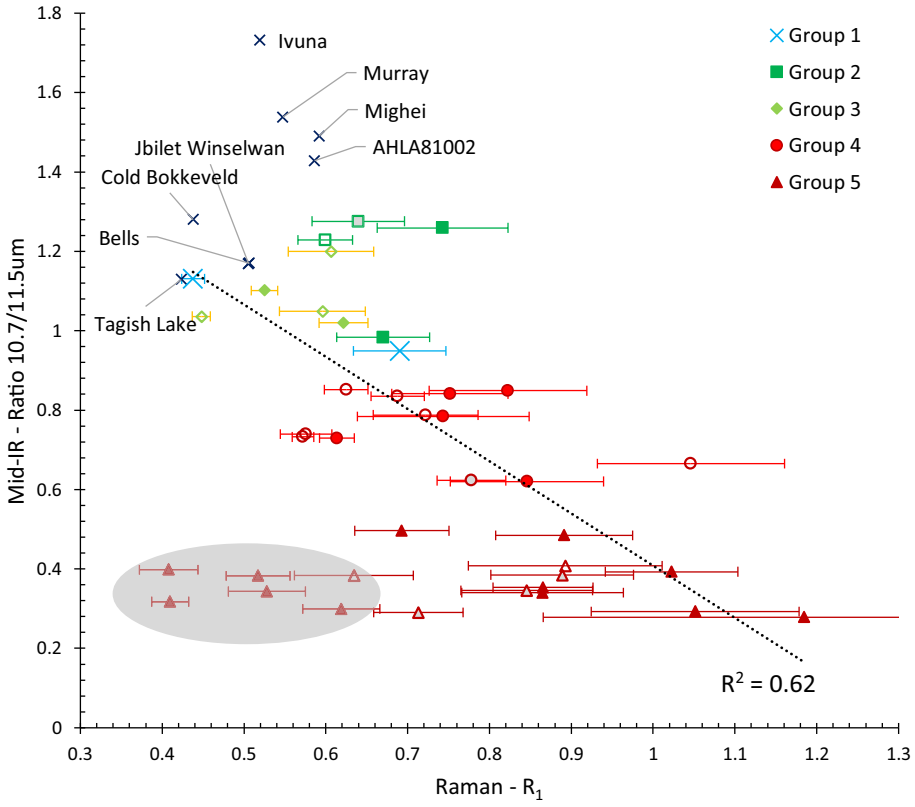

Fig. 8. Comparisons between mid-IR spectral groups and Raman R_1 peak height ratios. A moderate negative correlation (with an $R^2 = 0.62$) is observed between a sample's mid-IR ratio (or spectral group) and R_1 values. A small population (5) of group 5 FgMMs show anomalous R_1 values, which do not match the observed trend, these are considered in the discussion (4.3). In this plot spectral group are represented by different colours and shapes: blue crosses for group 1 MMs, purple crosses for chondrites, dark green squares for group 2, light green diamonds for group 3, red circles for group 4 and dark red triangles for group 5. In addition, solid fill denote C2-FgMMs, open shapes denote C1-FgMMs and grey-infilled shapes are ScMMs.

et al., 2001). FgMMs with relict textures and anhydrous matrices must have experienced minimum peak temperatures of 700 °C but not greater than ~1350 °C.

Cosmic spherules form at higher peak temperatures where significant melting and recrystallization has occurred. Although CS exhibit a wide range of textural types, each associated with different degrees of heating, they all record group 5 spectral signatures and contain (igneous) olivine as their major mineral. However, in glassy V-type CS the mid-IR spectra are indistinct, smooth reflectance profiles across the 10 μm region and this is attributed to either the amorphous nature of the mesostasis or a hyperfine grain size resulting in significant volume scattering. Mid-IR spectra cease to be useful metrics for the analysis of MM entry heating once partial melting has become significant.

4.2. Micrometeorite survival and atmospheric entry biases

In 2:1 phyllosilicates (e.g. hectorite, montmorillonite, nontronite, saponite and others) dehydroxylation reactions occur above 400 °C, with saponite exhibiting dehydroxylation between 600 and 700 °C; while 1:1 Kaolin group phyllosilicates, including serpentine, the major component of CM chondrites, are considerably more heat sensitive and begin dehydroxylation reactions at much lower temperatures, between 300 °C and 400 °C (Che and Glotch, 2012). This difference in temperature thresholds between 1:1 and 2:1 phyllosilicates were explored by Nozaki et al. (2006) and Akai (1992) within the context of natural and experimentally heated carbonaceous chondrites. Although the exact temperature thresholds for dehydroxylation reactions vary between studies, a common conclusion drawn is that CI chondrites bearing saponite are more heat resistant than CM bearing serpentine. Differences in the absolute temperature thresholds reported likely result from variation in the experimental procedure, with differences in heating duration and the associated kinetic effects of decomposition reactions playing a significant role. A higher temperature threshold is expected for 2:1 phyllosilicates than 1:1 phyllosilicates, this is because 2:1 structures contain inter-layer water while this is absent from 1:1 structures (Farmer, 1974; Bailey, 1980; Brown and Nadeau, 1984). Although natural CM chondrite samples may contain serpentine-like intermediate structures (e.g. antigorite and greenalite) which bear some interlayer water molecules (Tomeoka et al., 1989; Browning et al., 1996; Velbel and Palmer, 2011) the abundance of water is still considerably less than

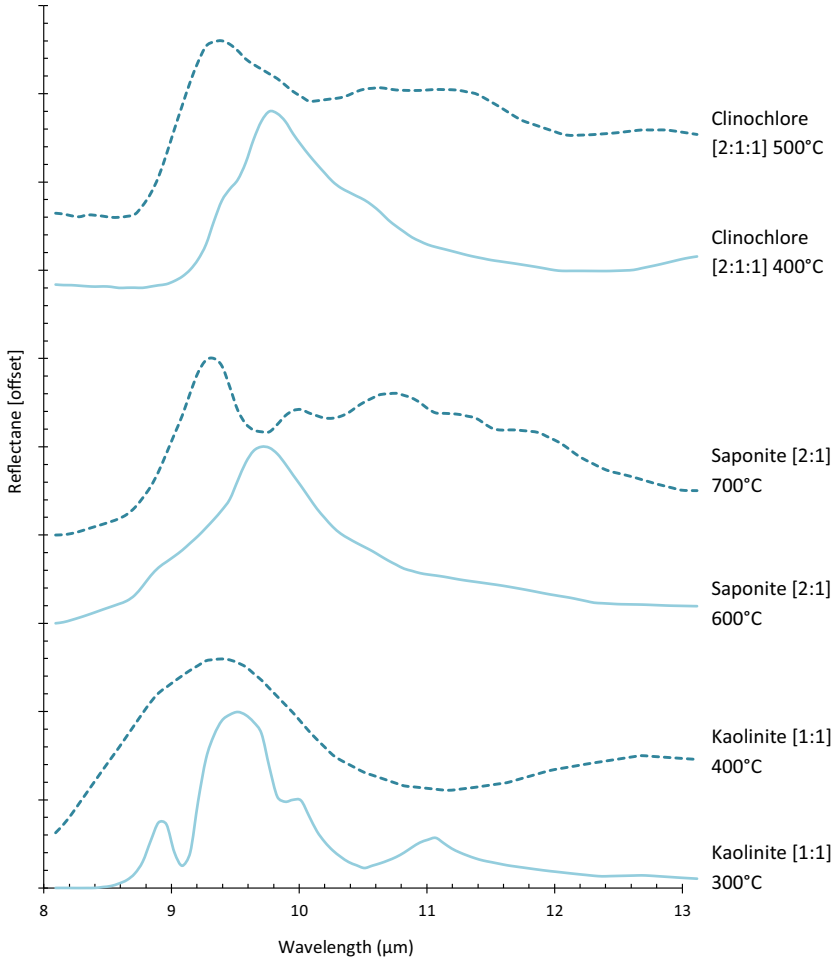

Fig. 9. The mid-IR evolution of selected phyllosilicate species during dehydroxylation. Spectra decompose from dehydrated sheet silicates to partially crystalline dehydroxylate mineraloids. Data are taken from Che and Glotch (2012). Kaolinite (1:1), saponite (2:1) and clinochlore (2:1:1) species are shown. However, the shift in primary peak positions is a characteristic feature for all other phyllosilicate species (not shown) within the 1:1, 2:1, and 2:1:1 families. Spectra are offset for clarity.

that held in true 2:1 structures such as saponite. Since dehydroxylation will only occur after dehydration, it follows that saponite will require higher temperatures (or longer duration heating) than serpentine before its volatile reservoir is expended and dehydroxylation reactions can occur.

A further disparity between the thermal decomposition behaviour of phyllosilicate species is seen in their cation chemistry. As outlined above, phyllosilicates progress through a standard thermal decomposition pathway from pristine sheet silicates to dehydrated then dehydroxylated phases before recrystallizing as anhydrous silicates; as temperatures rise further these annealed silicates will melt. Under the rapid heating experienced during atmosphere entry, disequilibrium melting will occur, and therefore the onset of melting will be dependent on both the bulk composition of the MM and the rate at which heat energy can be exchanged across the particle. The chemical composition of the groundmass will therefore partially control the melting point. The matrix of recrystallized unmelted FgMMs (those in spectral group 5) is composed of microcrystalline olivine, which will have retained the cation complement (either Mg-rich or Fe-rich) from their former phyllosilicate parents. The melting point of forsterite is extremely high, at ~1900 °C, however, substitution of Mg for Fe significantly lowers the melting point, such that Fe-rich fayalitic olivine melts at ~1200 °C. As a result the initial cation composition of phyllosilicates in a micrometeorite's matrix will be critical in defining the matrix solidus of the recrystallized anhydrous olivine. Micrometeorites bearing Fe-rich phyllosilicates, such as cronstedtite and ferrous saponite will have significantly lower solidus temperatures and consequently a lower unmelted survival rate than for particle containing Mg-rich phyllosilicates. Conversely, MMs with Mg-rich phyllosilicates will support a larger annealing temperature range and can therefore develop high crystallinity and coarser matrix grains whilst also being less likely to experience melting. Phyllosilicate cation chemistry is itself determined by the degree of aqueous alteration. Geochemical evidence suggests that with increasing aqueous alteration phyllosilicates evolve from Fe-bearing towards

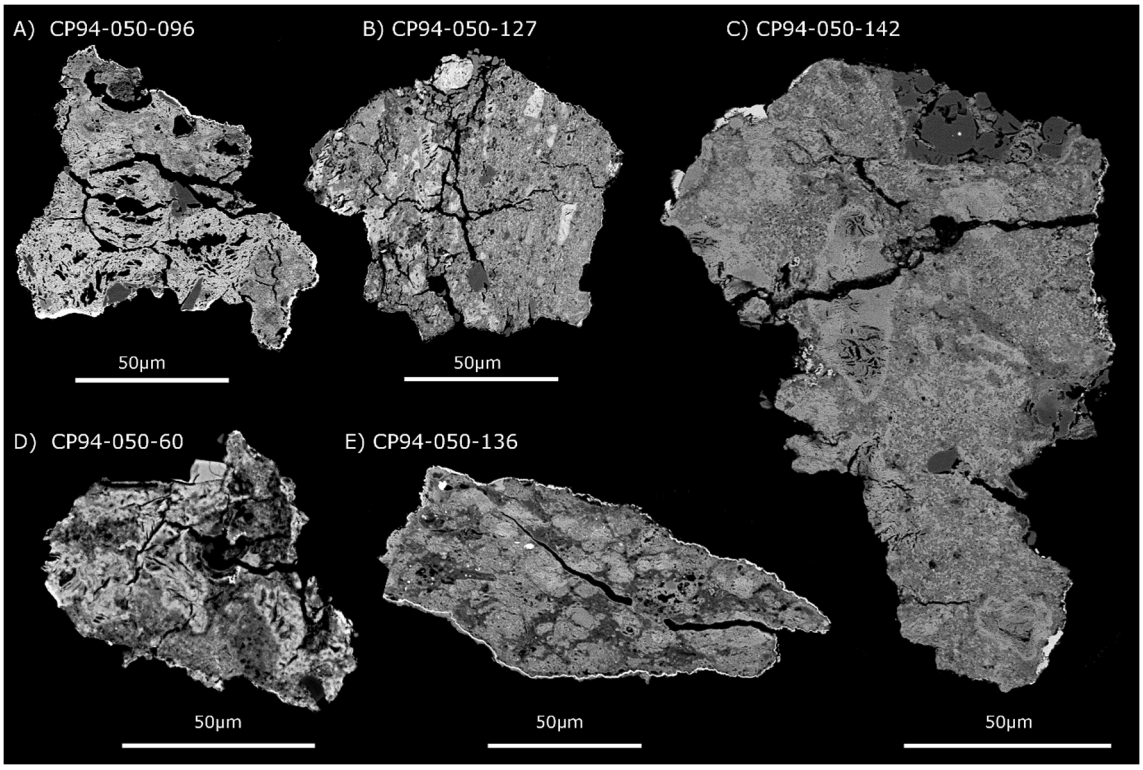

Fig. 10. BSE image panel illustrating 5 of the anomalous FgMMs from spectral group 5. Magnetite rims form only a partial covering and igneous rims are absent. Dehydration cracks may be present, as in CP94-050-060 and variations in the Z value of the matrix reflect a variable Mg/Fe cation composition over short distances, this is characteristic of CM lithologies and C2 FgMMs. Anhydrous olivines are common and some grains contain reduced metal droplets. The spectral profiles of these grains suggest their matrix has experienced complete recrystallization and consists of hyper-fine anhydrous olivine crystallites, however the Raman R_1 values of these grains are characteristic of only modestly heated chondritic materials, retaining a disordered carbonaceous signature. These two observations are contradictory, and not immediately reconcilable, possible explanations for this disparity are considered in the discussion Section 4.3.

Mg-rich end members (Howard et al., 2009). As a result the degree of aqueous alteration a MM has experienced on its parent body will define both the type of phyllosilicate species and the ratio of Fe:Mg cations in the phyllosilicate structure and therefore the probability of survival as an unmelted grain.

The observation that substantial differences will exist in the solidus temperatures of recrystallized FgMM groundmass have important implications for the analysis of MM parent bodies and collection statistics. Unmelted MM populations should preferentially preserve extensively aqueous altered CI-like, Mg-rich saponite bearing particles while Fe-cronstedtite bearing CM-like MMs will be preferentially melted to form unrecognisable ScMMs. However, the vast majority of unmelted FgMMs are instead C2 type with affinities to CM chondrites (Taylor et al., 2012). For C2 FgMMs to be the most common unmelted MM type, the relative flux of C1:C2 grains in the asteroid belt must be heavily skewed towards C2 dust. This would agree with observations from meteorite collection statistics which demonstrate that CM chondrites are the most abundant carbonaceous chondrite type recovered at ~43% (Burbine et al., 2002).

4.3. Anomalous group 5 FgMMs with an olivine groundmass

A small population (6) of the group 5 FgMMs, exhibit an anomalous Raman signature inconsistent with the mid-IR data which suggests high peak temperatures (>800 °C) sufficient to cause complete recrystallization of their matrix phyllosilicates into an olivine groundmass (see Fig. 8 for Raman R_1 data and Fig. 10 for BSE images of the anomalous group 5 FgMMs). At these temperatures the carbonaceous and organic phases, which appear in Raman spectra as 'G' and 'D' bands are expected to be either completely destroyed (absent) or extensively thermally reprocessed and consequently present with sharp peaks and high R_1 values (Dobrică et al., 2011). Instead the Raman signatures of the anomalous grains are preserved and suggest only modest heating (probably below 800 °C, similar to the peak temperatures of group 2 and 3 particles). Fig. 10 illustrates 5 of these anomalous grains, dehydration cracks are common, confirming that the matrix phyllosilicates have undergo dehydration reactions. However, igneous rims are absent and with the exception of CP94-050-136, particles show only a partial magnetite rim. In addition the relict matrix texture of these grains is

easily resolvable, often revealing former zones of coarse phyllosilicates, as well as distinct variations in the matrix cation chemistry, observation of such features allow their classification as C2-FgMMs. Conversely, the remaining group 5 FgMMs show vesicular matrix, inner igneous rims and complete outer magnetite rims, as well as a homogenised matrix with a uniform Z value under BSE, all features consistent with intense thermal reprocessing. Consequently, both the petrographic and Raman data suggest this anomalous population have experienced a different thermal history to that of the bulk group 5 population.

The atmospheric entry of hydrated FgMMs is known to progress by the melting of surface layers. This forms a melt which surrounds (and progressively consumes) an unmelted core. On cooling the surface melt crystallises to form an igneous rim (Genge, 2006). Since the thermal decomposition of phyllosilicates is an endothermic process, this reaction consumes much of the heat generated during atmospheric entry and therefore preserves the core from significant heating (Genge and Grady, 2000; Genge, 2006). The presence of hydrated phyllosilicates is therefore necessary for an igneous rim to form. Since our anomalous particles lack igneous rims this suggests these particles did not contain structural water and were therefore at least dehydroxylated prior to atmospheric entry. An anhydrous particle, of such a small size (~100 μm diameter), entering the atmosphere is expected be rapidly and evenly heated, this is because thermal conduction will efficiently transfer heat over short distances (Love and Brownlee, 1991); the resulting MM will be homogenously recrystallized. However, an outer spinel-magnetite rim is still expected to form as is observed in other anhydrous particles such as coarse-grained and scoriaceous MMs (Genge et al., 2008). This is because magnetite rims form by the progressive evaporation of volatile and moderately volatile elements and subsequent passive enrichment of the residual melt components which react with terrestrial oxygen and crystallise. Note that, with continued heating Fe in the melt layer will evaporate and magnetite rims are therefore not found on the intensely reprocessed CS (Toppani and Libourel, 2003; Genge et al., 2008).

In-space dehydroxylation requires the anomalous MMs to have a 2-stage thermal history with an initial period of heating on the C-type parent body, leading to dehydroxylation of the matrix phyllosilicates, before a second phase of heating during atmospheric entry, which would lead to the formation of a magnetite rim (since terrestrial oxygen is required) and the annealing of dehydroxylates into an olivine groundmass. The most likely source of parent body heating is impact events. Several thermally metamorphosed CM chondrites are now known which show both shock deformation and dehydrated (or dehydroxylated) phyllosilicates, these samples include Jbilet Winselwan (Zolensky et al., 2016), Sutter's Mill (Zolensky et al., 2014) and PCA 02012 (Nakato et al., 2013). These samples are interpreted as C-type regolith material. For this scenario to be plausible the carbonaceous phases detected by the Raman analysis would need to survive both episodes of heating.

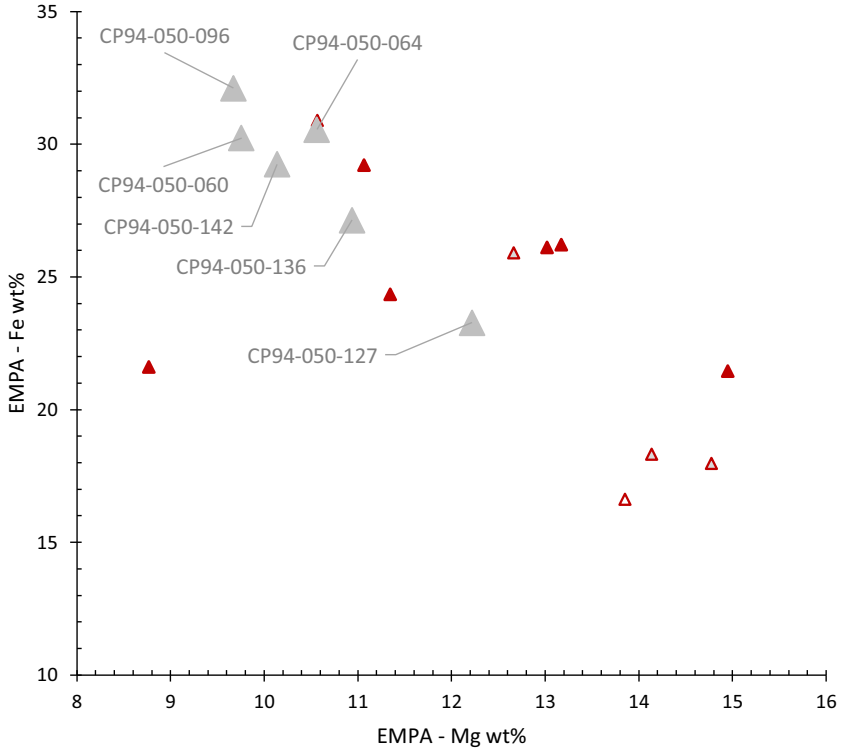

Fig. 11. Bulk matrix Mg vs. Fe abundances in group 5 FgMMs, calculated by EMPA. The anomalous grains (large grey triangles, labelled) tend to show higher Fe concentrations than their counterpart group 5 MMs with higher R_1 values. This suggests that Fe-enriched grains are more susceptible to heating and will undergo annealing reactions at lower temperatures than Mg-rich grains.

The peak temperatures associated with both events would therefore need to be relatively low. At present the peak temperature and duration of parent body thermal metamorphism on a CM parent body is poorly constrained and could have lasted for several days-1000's of years and ranged from 400 °C to 900 °C (Nakato et al., 2008; Davison et al., 2012; Tonui et al., 2014). Since carbonaceous phases have been detected by Raman microspectroscopy in several regolith CM samples, these phases can survive the moderate thermal conditions on their parent asteroid (Nakato et al., 2013). Conversely, atmospheric entry heating ranges from <600 °C to 2000 °C and typically lasts for 2–10 s (Love and Brownlee, 1991). However, if atmospheric entry heating was below the maximum temperature of parent body heating then the carbonaceous phases could also survive entry unaltered. This of course would occur only in a low number of particles, since the average peak temperature experienced by a 100 μm diameter particles is around 1350 °C (Love and Brownlee, 1991). Therefore most of the dehydroxylated FgMMs would experience higher temperatures and melt, forming unrecognisable scoriaceous MMs or CS.

The olivine groundmass in the anomalous group 5 FgMMs also show an Fe-enriched composition, with higher Fe concentrations than most, but not all, of the group 5 FgMMs (this is shown in Fig. 11). It is therefore probable that the matrix phyllosilicates in the anomalous FgMMs were predominantly Fe-cronstedtite. In Section 4.2, we outlined how Fe-bearing phyllosilicates are the most susceptible to heating and will undergo dehydroxylation reactions at temperatures as low as ~300–400 °C and experience annealing at temperatures around ~700 °C. Where pre-existing relict anhydrous olivine grains are present in the matrix these may also act as nucleation points and encourage recrystallization at even lower temperatures.

Given the evidence above, which includes unusually low R_1 Raman values - suggesting relatively low (<800 °C) peak temperatures, Fe-rich bulk compositions – which are susceptible to thermal decomposition, and the absence of igneous rims – which implies the anomalous group 5 FgMMs were anhydrous prior to atmospheric entry, we suggest that the anomalous grains most likely represent pre-atmospheric dehydroxylated CM-like chondritic dust recovered from the regolith of a C-type asteroid.

5. IMPLICATIONS

5.1. Dehydroxylated micrometeorites may be ideal samples for spectroscopic comparisons with C-type asteroids

This study has demonstrated how the conversion of matrix phyllosilicates to dehydroxylates is an important intermediate stage in the thermal evolution of all hydrated chondritic materials. Dehydroxylates are metastable over a wide temperature range (~300–800 °C) and subsequently recrystallize as fine-grained metamorphic olivine. This process is known to occur both during atmospheric entry and in the surface layers of C-type asteroids. Abundant evidence suggests that the vast majority of fine-grained micrometeorites remain hydrated during liberation from

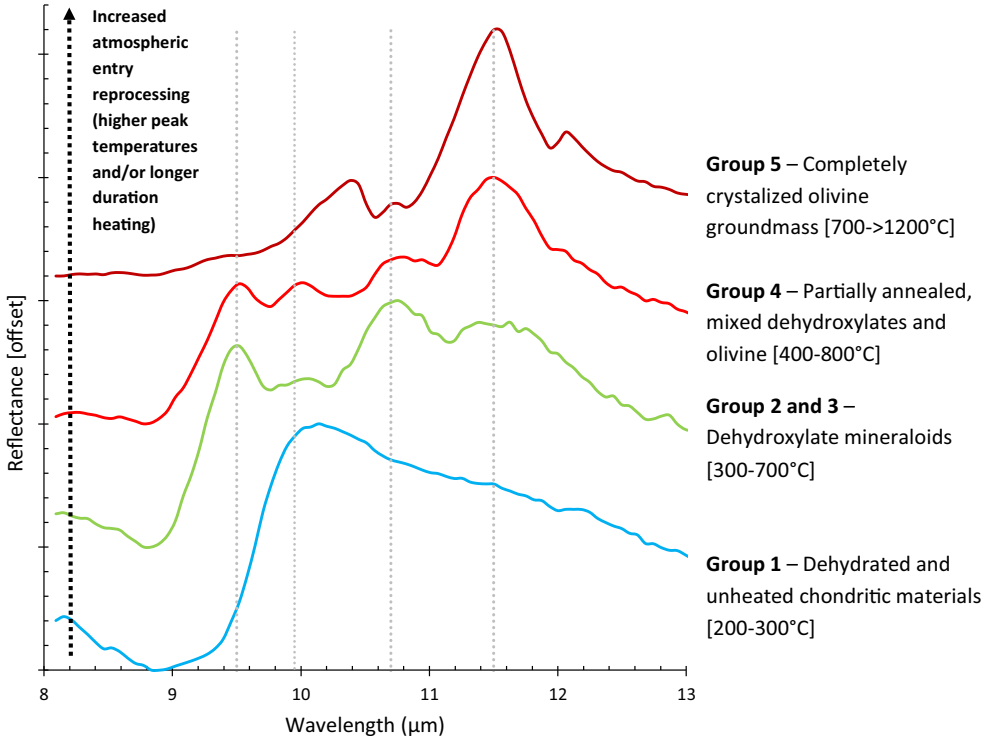

Fig. 12. The mid-IR spectral evolution of hydrated chondritic material with heating (during atmospheric entry). Despite compositional differences between CM and CI-like FgMMs both groups follow the same generic spectral decomposition pathway defined by the stability of phyllosilicate phases and dependent on their composition and cation chemistry. Dashed grey lines show the positions of the main Reststrahlen band reflectance peaks present in heated MMs.

their parent asteroid (Nakamura et al., 2001; Noguchi et al., 2002; Genge, 2006) and are then thermally decomposed during atmospheric entry. However, the identification of 6 anomalous grains whose combined petrographic and Raman data suggests they have experienced in-space dehydroxylation provide support for the conclusion that (at least some) micrometeorites are dehydroxylated in space. These rare grains are the first positively identified regolith micrometeorites and, therefore, complement the increasing collections of thermally metamorphosed CM chondrites (Nakato et al., 2013; Zolensky et al., 2014, 2016). Consequently, fine-grained micrometeorites act as both analogue materials for, and direct sample returns from the surfaces of C-type asteroids.

This study identified a prominent reflectance peak at 9.0–9.5 μm in the mid-IR spectra of dehydroxylated fine-grained micrometeorites. This feature is associated with stretching of Si–O bonds in residual, isolated silica tetrahedra. Since this peak is unlike the signatures derived from hydrated or anhydrous silicates, this spectroscopic feature may provide a new and diagnostic tool with which to analyse asteroid surfaces. However, because asteroid surface spectra are derived from emission spectra (Emery et al., 2006; Vernazza et al., 2012; Landsman et al., 2016) this dehydroxylate feature will, instead, appear as a trough, as dictated by Kirchhoff's Emissivity Law ($\varepsilon = 1\text{-}R$) (Salisbury et al., 1994; Che and Glotch, 2012). We predict that a 9.0–9.5 μm trough will be present in the spectra of many young C-type asteroids, which have remained unaffected by space weathering.

5.2. Textural classification of micrometeorites

The recrystallized olivine groundmass in thermally decomposed, but unmelted grains preserves both earlier stages of decomposition (such as dehydration cracks) as well as the pre-atmospheric parent body textures. As a result even severely heated and reprocessed (group 4 and 5) grains will preserve their pre-atmospheric parent body textures, allowing their classification. Furthermore, this observation means that BSE images alone are insufficient evidence on which to characterise the degree of atmospheric entry reprocessing a micrometeorite has experienced. If a micrometeorite is classified using only this data the conclusion of heat processing is likely to lead to lower than expected peak temperature estimates. Instead, mid-IR spectra are required to determine what mineral compose the matrix/groundmass.

6. CONCLUSIONS

Upon impact with the Earth's upper atmosphere, micrometeorites composed of hydrated phyllosilicates experience flash heating and thermal decomposition. This process can be described by a generic 4-stage mid-IR spectral evolution. Initially inter-layer water is lost causing contraction of sheet silicates and dehydration cracks to form. The latter process, may be responsible for the fragmentation of some friable grains. However, no mid-IR spectroscopic change accompanies this structural rearrangement. With further heating water bonded to octahedral layers is lost in condensation reactions and dehydroxylate mineraloids form. This leads to significant spectral changes. A relatively sharp, mid-IR reflectance peak appears at 9.0–9.5 μm relating to the dehydroxylate structure. The majority of unmelted fine-grained micrometeorites (~57%) contain this spectral signature. With continued heating and higher peak temperatures dehydroxylate mineraloids experience solid-state recrystallization, forming a hyperfine (metamorphic) olivine groundmass. This groundmass tends to preserve both earlier thermal decomposition features, namely dehydration cracks, as well as pre-atmospheric parent body textures, allowing the identification of parent body signatures even among thermally reprocessed grains. In the final stages of thermal decomposition recrystallized olivine melts (above 1200–1350 °C) and mesostasis (igneous) olivine forms. Mid-IR data (shown in Fig. 12) demonstrates the generic spectroscopic profiles for each stage and assigns estimated temperature ranges. This decomposition pathway was constructed on the basis of experimentally heated phyllosilicates, by Che and Glotch (2012) and empirical observations of a large fine-grained micrometeorite population in the mid-IR. The absolute temperature at which each decomposition stage occurs is highly dependent on the species of phyllosilicate and its cation chemistry. Intensely aqueously altered Mg-bearing saponite is significantly more heat resistant than Fe-bearing serpentine. Atmospheric entry should, therefore, bias the survival of micrometeorites in favour of CI-like grains. However, both micrometeorite and (macro)meteorite populations contain abundantly more (2–4x) CM chondrites and CM-like micrometeorites, implying that CI parent bodies are significantly rarer than CM parent bodies in the asteroid belt. Finally, this study revealed the presence of a small population of anomalous fine-grained micrometeorites which lack igneous rims, retain disordered carbonaceous matter, contain an Fe-rich bulk composition and are composed of recrystallized olivine. This population may represent in-space dehydroxylated micrometeorites, sourced from the regolith of C-type asteroids.

ACKNOWLEDGEMENTS

The data presented in this paper were acquired during M. Suttle's PhD research and funded by the Science and Technology Council (STFC) under a training grant scheme (Grant Number ST/M503526/1) and in association with Imperial College London. M. Genge is funded by the STFC [Grant Number ST/J001260/1], S. Russell is funded by the STFC (Grant Number ST/M00094X/1) and L. Folco is funded by the Italian Programma Nazionale delle Ricerche in Antartide (PNRA) through the Meteoriti Antartiche project (Grant Number PNRA16_00029_A1). We thank Diamond Light Source for access to the spectroscopy support and characterisation lab (91) and Dr. Tina Geriaki for help with analytical acquisition. Additionally, the NHM, London and N. Almedia, are thanked for the loan of meteorite samples. We are grateful to Dr. Pierre Beck for editorial handling and to Eric Quirico and 2 anonymous reviewers for their constructive comments.

APPENDIX A. SUPPLEMENTARY MATERIAL

Supplementary data associated with this article can be found, in the online version, at http://dx.doi.org/10.1016/j.gca.2017.03.002.

REFERENCES

Akai J. (1992) TTT diagram of serpentine and saponite, and estimation of metamorphic heating degree of Antarctic carbonaceous chondrites. *Antarct. Meteorite Res.* **5**, 120–135.

Alexander C. M. D., Taylor S., Delaney J. S., Ma P. and Herzog G. F. (2002) Mass-dependent fractionation of Mg, Si, and Fe isotopes in five stony cosmic spherules. *Geochim. Cosmochim. Acta* **66**, 173–183.

Bailey S. W. (1980) Structures of layer silicates. In *Crystal Structures of Clay Minerals and their X-ray Identification* (eds. G. W. Brindley and G. Brown). Mineralogical Society, London, pp. 1–124.

Beck P., Quirico E., Montes-Hernandez G., Bonal L., Bollard J., Orthous-Daunay F. R., Howard K. T., Schmitt B., Brissaud O., Deschamps F. and Wunder B. (2010) Hydrous mineralogy of CM and CI chondrites from infrared spectroscopy and their relationship with low albedo asteroids. *Geochim. Cosmochim. Acta* **74**, 4881–4892.

Beck P., Garenne A., Quirico E., Bonal L., Montes-Hernandez G., Moynier F. and Schmitt B. (2014) Transmission infrared spectra (2–25 μm) of carbonaceous chondrites (CI, CM, CV–CK, CR, C2 ungrouped): mineralogy, water, and asteroidal processes. *Icarus* **229**, 263–277.

Bonal L., Quirico E., Bourot-Denise M. and Montagnac G. (2006) Determination of the petrologic type of CV3 chondrites by Raman spectroscopy of included organic matter. *Geochim. Cosmochim. Acta* **70**, 1849–1863.

Brown G. and Nadeau P. (1984) Crystal structures of clay minerals and related phyllosilicates [and discussion]. *Philos. Trans. Roy. Soc. Lond. A Math. Phys. Eng. Sci.* **311**, 221–240.

Browning L. B., McSween H. Y. and Zolensky M. E. (1996) Correlated alteration effects in CM carbonaceous chondrites. *Geochim. Cosmochim. Acta* **60**, 2621–2633.

Brownlee D. E., Bates B. and Schramm L. (1997) The elemental composition of stony cosmic spherules. *Meteoritics Planet. Sci.* **32**, 157–175.

Brunetto R., Borg J., Dartois E., Rietmeijer F. J. M., Grossemy F., Sandt C., d'Hendecourt L. L. S., Rotundi A., Dumas P., Djouadi Z. and Jamme F. (2011) Mid-IR, Far-IR, Raman micro-spectroscopy, and FESEM–EDX study of IDP L2021C5: clues to its origin. *Icarus* **212**, 896–910.

Burbine T. H., McCoy T. J., Meibom A., Gladman B. and Keil K. (2002) Meteoritic parent bodies: their number and identification. In *Asteroids III*. Arizona Univ. Press, Arizona, pp. 653–667.

Busemann H., Alexander M. D. and Nittler L. R. (2007) Characterization of insoluble organic matter in primitive meteorites by microRaman spectroscopy. *Meteoritics Planet. Sci.* **42**, 1387–1416.

Campins H., Hargrove K., Pinilla-Alonso N., Howell E. S., Kelley M. S., Licandro J., Mothé-Diniz T., Fernández Y. and Ziffer J. (2010) Water ice and organics on the surface of the asteroid 24 Themis. *Nature* **464**, 1320–1321.

Carrillo-Sánchez J. D., Plane J. M. C., Feng W., Nesvorný D. and Janches D. (2015) On the size and velocity distribution of cosmic dust particles entering the atmosphere. *Geophys. Res.* **42**, 6518–6525.

Caro G. M., Dartois E. and Nakamura-Messenger K. (2008) Characterization of the carbon component in cometary Stardust samples by means of infrared and Raman spectroscopy. *Astron. Astrophys.* **485**, 743–751.

Che C. and Glotch T. D. (2012) The effect of high temperatures on the mid-to-far-infrared emission and near-infrared reflectance spectra of phyllosilicates and natural zeolites: implications for Martian exploration. *Icarus* **218**, 585–601.

Cordier C. and Folco L. (2014) Oxygen isotopes in cosmic spherules and the composition of the near Earth interplanetary dust complex. *Geochim. Cosmochim. Acta* **146**, 18–26.

Dartois E., Engrand C., Brunetto R., Duprat J., Pino T., Quirico E., Remusat L., Bardin N., Briani G., Mostefaoui S. and Morinaud G. (2013) Ultra carbonaceous antarctic micrometeorites, probing the Solar System beyond the nitrogen snow-line. *Icarus* **224**, 243–252.

Davison T. M., Ciesla F. J. and Collins G. S. (2012) Post-impact thermal evolution of porous planetesimals. *Geochim. Cosmochim. Acta* **95**, 252–269.

Dobrică E., Engrand C., Quirico E., Montagnac G. and Duprat J. (2011) Raman characterization of carbonaceous matter in CONCORDIA Antarctic micrometeorites. *Meteoritics Planet. Sci.* **46**, 1363–1375.

Dobrică E., Engrand C., Leroux H., Rouzaud J. N. and Duprat J. (2012) Transmission electron microscopy of CONCORDIA ultracarbonaceous Antarctic micrometeorites (UCAMMs): mineralogical properties. *Geochim. Cosmochim. Acta* **76**, 68–82.

Drits V. A. and McCarty D. K. (2007) The nature of structure-bonded H_2O in illite and leucophyllite from dehydration and dehydroxylation experiments. *Clays Clay Min.* **55**, 45–58.

Emery J. P., Cruikshank D. P. and van Cleve J. (2006) Thermal emission spectroscopy (5.2–38 μm) of three Trojan asteroids with the Spitzer Space Telescope: detection of fine-grained silicates. *Icarus* **182**, 496–512.

Engrand C., McKeegan K. D. and Leshin L. A. (1999) Oxygen isotopic compositions of individual minerals in Antarctic micrometeorites: Further links to carbonaceous chondrites. *Geochim. Cosmochim. Acta* **63**, 2623–2636.

Feierberg M. A., Lebofsky L. A. and Tholen D. J. (1985) The nature of C-class asteroids from 3-μm spectrophotometry. *Icarus* **63**, 183–191.

Farmer V. C. (1974) The layer silicates. In *The Infrared Spectra of Minerals* (ed. V. C. Farmer). Mineralogical Society, London, pp. 331–363.

Flynn G. J., Durda D. D., Sandel L. E., Kreft J. W. and Strait M. M. (2009) Dust production from the hypervelocity impact disruption of the Murchison hydrous CM2 meteorite: Implications for the disruption of hydrous asteroids and the production of interplanetary dust. *Planet. Space Sci.* **57**, 119–126.

Fornasier S., Lantz C., Perna D., Campins H., Barucci M. A. and Nesvorný D. (2016) Spectral variability on primitive asteroids of the Themis and Beagle families: space weathering effects or parent body heterogeneity? *Icarus* **269**, 1–14.

Gardner J. P., Mather J. C., Clampin M., Doyon R., Greenhouse M. A., Hammel H. B., Hutchings J. B., Jakobsen P., Lilly S. J., Long K. S. and Lunine J. I. (2006) The James Webb space telescope. *Space Sci. Rev.* **123**, 485–606.

Genge M. J., Grady M. M. and Hutchison R. (1997) The textures and compositions of fine-grained Antarctic micrometeorites: implications for comparisons with meteorites. *Geochim. Cosmochim. Acta* **61**, 5149–5162.

Genge, M. J. and Grady, M. M. (2000) The thermal evolution of micrometeoroids during atmospheric entry. *Lunar Planet. Sci. XXXI. Lunar Planet. Inst., Houston. #1361(abstr.)*.

Genge M. J., Bradley J. P., Engrand C., Gounelle M., Harvey R. P. and Grady M. M. (2001) The petrology of fine-grained

micrometeorites: evidence for the diversity of primitive asteroids. *Lunar Planet. Sci. XXXII. Lunar Planet. Inst., Houston. #1546(abstr.)*.

Genge M. J., Gileski A. and Grady M. M. (2005) Chondrules in Antarctic micrometeorites. *Meteoritics Planet. Sci.* **40**, 225–238.

Genge M. J. (2006) Igneous rims on micrometeorites. *Geochim. Cosmochim. Acta* **70**, 2603–2621.

Genge M. J. (2007) Evidence for Shock in Micrometeorites. In *70th Annual Meeting of the Meteoritical Society, held August 13–17*. Tucson, Arizona, #5007(abstr.).

Genge M. J. (2008) Micrometeorites and their implications for meteors. *Earth Moon Planets* **102**, 525–535.

Genge M. J., Engrand C., Gounelle M. and Taylor S. (2008) The classification of micrometeorites. *Meteoritics Planet. Sci.* **43**, 497–515.

Gonczi R. and Froeschlé C. (1982) Poynting-Robertson drag and orbital resonance. *Icarus* **51**, 633–654.

Gounelle M., Chaussidon M., Morbidelli A., Barrat J. A., Engrand C., Zolensky M. E. and McKeegan K. D. (2009) A unique basaltic micrometeorite expands the inventory of solar system planetary crusts. *Proc. Natl. Acad. Sci.* **106**, 6904–6909.

Greshake A., Kloeck W., Arndt P., Maetz M., Flynn G. J., Bajt S. and Bischoff A. (1998) Heating experiments simulating atmospheric entry heating of micrometeorites: clues to their parent body sources. *Meteoritics Planet. Sci.* **33**, 267–290.

Grossman J. N. and Brearley A. J. (2005) The onset of metamorphism in ordinary and carbonaceous chondrites. *Meteoritics Planet. Sci* **40**, 87–122.

Hallenbeck S. L., Nuth J. A. and Daukantas P. L. (1998) Mid-infrared spectral evolution of amorphous magnesium silicate smokes annealed in vacuum: comparison to cometary spectra. *Icarus* **131**, 198–209.

Hanowski N. P. and Brearley A. J. (2001) Aqueous alteration of chondrules in the CM carbonaceous chondrite, Allan Hills 81002: implications for parent body alteration. *Geochim. Cosmochim. Acta* **65**, 495–518.

Hargrove K. D., Emery J. P., Campins H. and Kelley M. S. (2015) Asteroid (90) antiope: another icy member of the themis family? *Icarus* **254**, 150–156.

Harker D. E., Woodward C. E., Kelley M. S., Sitko M. L., Wooden D. H., Lynch D. K. and Russell R. W. (2010) Mid-infrared spectrophotometric observations of fragments B and C of Comet 73P/Schwassmann-Wachmann 3. *Astron. J.* **141**, 26.

Herter T. L., Adams J. D., De Buizer J. M., Gull G. E., Schoenwald J., Henderson C. P., Keller L. D., Nikola T., Stacey G. and Vacca W. D. (2012) First science observations with SOFIA/FORCAST: the FORCAST mid-infrared camera. *Astrophys. J. Lett.* **749**, L18.

Hartmann W. K., Tholen D. J. and Cruikshank D. P. (1987) The relationship of active comets, "extinct" comets, and dark asteroids. *Icarus* **69**, 33–50.

Houck J. R., Roellig T. L., van Cleve J., Forrest W. J., Herter T., Lawrence C. R., Matthews K., Reitsema H. J., Soifer B. T., Watson D. M. and Weedman D. (2004) The infrared spectrograph (IRS) on the Spitzer space telescope. *Astrophys. J. Suppl.* **154**, 18–24.

Howard K. T., Benedix G. K., Bland P. A. and Cressey G. (2009) Modal mineralogy of CM2 chondrites by X-ray diffraction (PSD-XRD). Part 1: Total phyllosilicate abundance and the degree of aqueous alteration. *Geochim. Cosmochim. Acta* **73**, 4576–4589.

Howard K. T., Benedix G. K., Bland P. A. and Cressey G. (2011) Modal mineralogy of CM chondrites by X-ray diffraction (PSD-XRD): Part 2. Degree, nature and settings of aqueous alteration. *Geochim. Cosmochim. Acta* **75**, 2735–2751.

Imae N. (2012) Cometary dust in Antarctic micrometeorites. *Proc. Internat. Astron. Union* **8**, 123–129.

Janches D., Mathews J. D., Meisel D. D., Getman V. S. and Zhou Q. H. (2000) Doppler studies of near-antapex UHF radar micrometeors. *Icarus* **143**, 347–353.

Kagi H., Tsuchida I., Wakatsuki M., Takahashi K., Kamimura N., Iuchi K. and Wada H. (1994) Proper understanding of down-shifted Raman spectra of natural graphite: direct estimation of laser-induced rise in sample temperature. *Geochim. Cosmochim. Acta* **58**, 3527–3530.

Kieffer S. W. (1979) Thermodynamics and lattice vibrations of minerals: 2. Vibrational characteristics of silicates. *Rev. Geophys.* **17**, 20–34.

Koike C., Mutschke H., Suto H., Naoi T., Chihara H., Henning T., Jäger C., Tsuchiyama A., Dorschner J. and Okuda H. (2006) Temperature effects on the mid-and far-infrared spectra of olivine particles. *Astron. Astrophys.* **449**, 583–596.

Kurat G., Koeberl C., Presper T., Brandstätter F. and Maurette M. (1994) Petrology and geochemistry of Antarctic micrometeorites. *Geochim. Cosmochim. Acta* **58**, 3879–3904.

Landsman Z. A., Licandro J., Campins H., Ziffer J., de Prá M. and Cruikshank D. P. (2016) The Veritas and Themis asteroid families: 5–14μm spectra with the Spitzer space telescope. *Icarus* **269**, 62–74.

Love S. G. and Brownlee D. E. (1991) Heating and thermal transformation of micrometeoroids entering the Earth's atmosphere. *Icarus* **89**, 26–43.

Love S. G. and Brownlee D. E. (1993) A direct measurement of the terrestrial mass accretion rate of cosmic dust. *Science* **262**, 550–553.

Madejová J. (2003) FTIR techniques in clay mineral studies. *Vib. Spectrosc.* **31**, 1–10.

Maurette M., Olinger C., Michel-Levy M. C., Kurat G., Pourchet M., Brandstätter F. and Bourot-Denise M. (1991) A collection of diverse micrometeorites recovered from 100 tonnes of Antarctic blue ice. *Nature* **351**, 44–47.

Maurette M., Immel G., Hammer C., Harvey R., Kurat G. and Taylor S. (1994) Collection and curation of IDPs from the Greenland and Antarctic ice sheets. *AIP Conf. Proc.* **310**, 277–290.

Miyamoto M. and Zolensky M. E. (1994) Infrared diffuse reflectance spectra of carbonaceous chondrites: amount of hydrous minerals. *Meteoritics* **29**, 849–853.

Nakamura T., Noguchi T., Yada T., Nakamuta Y. and Takaoka N. (2001) Bulk mineralogy of individual micrometeorites determined by X-ray diffraction analysis and transmission electron microscopy. *Geochim. Cosmochim. Acta* **65**, 4385–4397.

Nakamura T. (2005) Post-hydration thermal metamorphism of carbonaceous chondrites. *J. Min. Petrol. Sci.* **100**, 260–272.

Nakato A., Nakamura T., Kitajima F. and Noguchi T. (2008) Evaluation of dehydration mechanism during heating of hydrous asteroids based on mineralogical and chemical analysis of naturally and experimentally heated CM chondrites. *Earth Planets Space* **60**, 855–864.

Nakato A, Brearley A. J., Nakamura T., Noguchi T., Ahn I., Lee J. I., Matsuoka M. and Sasaki S. (2013). PCA 02012: A unique thermally metamorphosed carbonaceous chondrite. *Lunar Planet. Sci. XXXXIV. Lunar Planet. Inst., Houston. #2708 (abstr.)*.

Nazarov M. A., Kurat G., Brandstaetter F., Ntaflos T., Chaussidon M. and Hoppe P. (2009) Phosphorus-bearing sulfides and their associations in CM chondrites. *Petrology* **17**, 101–123.

Nesvorný D., Bottke W. F., Levison H. F. and Dones L. (2003) Recent origin of the solar system dust bands. *Astrophys. J.* **591**, 486–497.

Nesvorný D., Vokrouhlický D., Bottke W. F. and Sykes M. (2006) Physical properties of asteroid dust bands and their sources. *Icarus* **181**, 107–144.

Nesvorný D., Jenniskens P., Levison H. F., Bottke W. F., Vokrouhlický D. and Gounelle M. (2010) Cometary origin of the zodiacal cloud and carbonaceous micrometeorites. Implications for hot debris disks. *Astrophys. J.* **713**, 816.

Noguchi T., Nakamura T. and Nozaki W. (2002) Mineralogy of phyllosilicate-rich micrometeorites and comparison with Tagish Lake and Sayama meteorites. *Earth Planet. Sci. Lett.* **202**, 229–246.

Noguchi T., Ohashi N., Tsujimoto S., Mitsunari T., Bradley J. P., Nakamura T., Toh S., Stephan T., Iwata N. and Imae N. (2015) Cometary dust in Antarctic ice and snow: past and present chondritic porous micrometeorites preserved on the Earth's surface. *Earth Planet. Sci. Lett.* **410**, 1–11.

Nozaki W., Nakamura T. and Noguchi T. (2006) Bulk mineralogical changes of hydrous micrometeorites during heating in the upper atmosphere at temperatures below 1000 °C. *Meteoritics Planet. Sci.* **41**, 1095–1114.

Osawa T., Kagi H. and Nagao K. (2001) Mid-infrared transmission spectra of individual Antarctic micrometeorites and carbonaceous chondrites. *Antarctic Meteorite res.* **14**, 71–88.

Ostrowski D. R., Gietzen K., Lacy C. and Sears D. W. (2010) An investigation of the presence and nature of phyllosilicates on the surfaces of C asteroids by an analysis of the continuum slopes in their near-infrared spectra. *Meteoritics Planet. Sci.* **45**, 615–637.

Peucker-Ehrenbrink B. (1996) Accretion of extraterrestrial matter during the last 80 million years and its effect on the marine osmium isotope record. *Geochim. Cosmochim. Acta* **60**, 3187–3196.

Poynting J. H. (1904) Radiation in the solar system: its effect on temperature and its pressure on small bodies. *Philos. Trans. Roy. Soc. London. Ser. A Containing Pap. Math. Physical Char.* **202**, 525–552.

Prasad M. S., Rudraswami N. G. and Panda D. K. (2013) Micrometeorite flux on Earth during the last ~50,000 years. *J. Geophys. Res. Planets* **118**, 2381–2399.

Prost R. (1973) The influence of the Christiansen effect on IR spectra of powders. *Clays Clay Min* **21**, 363–368.

Quirico E., Orthous-Daunay F. R., Beck P., Bonal L., Brunetto R., Dartois E., Pino T., Montagnac G., Rouzaud J. N., Engrand C. and Duprat J. (2014) Origin of insoluble organic matter in type 1 and 2 chondrites: new clues, new questions. *Geochim. Cosmochim. Acta* **136**, 80–99.

Rahl J. M., Anderson K. M., Brandon M. T. and Fassoulas C. (2005) Raman spectroscopic carbonaceous material thermometry of low-grade metamorphic rocks: calibration and application to tectonic exhumation in Crete, Greece. *Earth Planet. Sci. Lett.* **240**, 339–354.

Rinaldi R. and Llovet X. (2015) Electron probe microanalysis: a review of the past, present, and future. *Microscopy Microanal.* **21**, 1053–1069.

Rochette P., Folco L., Suavet C., van Ginneken M., Gattacceca J., Perchiazzi N., Braucher R. and Harvey R. P. (2008) Micrometeorites from the transantarctic mountains. *Proc. Natl. Acad. Sci.* **105**, 18206–18211.

Rubin A. E., Trigo-Rodríguez J. M., Huber H. and Wasson J. T. (2007) Progressive aqueous alteration of CM carbonaceous chondrites. *Geochim. Cosmochim. Acta* **71**, 2361–2382.

Salisbury J. W., D'Aria D. M. and Jarosewich E. (1991) Midinfrared (2.5–13.5 μm) reflectance spectra of powdered stony meteorites. *Icarus* **92**, 280–297.

Salisbury J. W. and Wald A. (1992) The role of volume scattering in reducing spectral contrast of reststrahlen bands in spectra of powdered minerals. *Icarus* **96**, 121–128.

Salisbury J. W. (1993) Mid-infrared spectroscopy: laboratory data. In *Remote Geochemical Analysis: Elemental and Mineralogical Composition* (eds. C. M. Pieters and P. A. J. Englert). Cambridge Univ. Press, pp. 68–79.

Salisbury J. W., Wald A. and D'Aria D. M. (1994) Thermal-infrared remote sensing and Kirchhoff's law: 1. Laboratory measurements. *J. Geophys. Res. Solid Earth* **99**, 11897–11911.

Sandford S. A. (1984) Infrared transmission spectra from 2.5 to 25 μm of various meteorite classes. *Icarus* **60**, 115–126.

Schulz R., Stüwe J. A. and Boehnhardt H. (2004) Rosetta target comet 67P/Churyumov-Gerasimenko-Postperihelion gas and dust production rates. *Astron. Astrophys.* **422**, L19–L21.

Schulz R., Hilchenbach M., Langevin Y., Kissel J., Silen J., Briois C., Engrand C., Hornung K., Baklouti D., Bardyn A. and Cottin H. (2015) Comet 67P/Churyumov-Gerasimenko sheds dust coat accumulated over the past four years. *Nature* **518**, 216–218.

Speck A. K., Whittington A. G. and Hofmeister A. M. (2011) Disordered silicates in space: a study of laboratory spectra of "amorphous" silicates. *Astrophys. J.* **740**, 93–110.

Steele I. M. (1992) Olivine in Antarctic micrometeorites: comparison with other extraterrestrial olivine. *Geochim. Cosmochim. Acta* **56**, 2923–2929.

Suavet C., Rochette P., Kars M., Gattacceca J., Folco L. and Harvey R. P. (2009) Statistical properties of the Transantarctic Mountains (TAM) micrometeorite collection. *Polar Sci.* **3**, 100–109.

Suavet C., Alexandre A., Franchi I. A., Gattacceca J., Sonzogni C., Greenwood R. C., Folco L. and Rochette P. (2010) Identification of the parent bodies of micrometeorites with high-precision oxygen isotope ratios. *Earth Planet. Sci. Lett.* **293**, 313–320.

Suttle M. D., van Ginneken M. and Genge M. J. (2015). Larkman Nunatak micrometeorites, a statistical study. *Meteoritical Society LXXVIII. San Francisco. #5063(abstr.)*.

Suzuki A., Yamanoi Y., Nakamura T. and Nakashima S. (2010) Micro-spectroscopic characterization of organic and hydrous components in weathered Antarctic micrometeorites. *Earth Planets Space* **62**, 33–46.

Takir D., Emery J. P., Mcsween H. Y., Hibbitts C. A., Clark R. N., Pearson N. and Wang A. (2013) Nature and degree of aqueous alteration in CM and CI carbonaceous chondrites. *Meteoritics Planet. Sci.* **48**, 1618–1637.

Taylor S., Lever J. H. and Harvey R. P. (1998) Accretion rate of cosmic spherules measured at the South Pole. *Nature* **392**, 899–903.

Taylor S., Jones K. W., Herzog G. F. and Hornig C. E. (2011) Tomography: a window on the role of sulfur in the structure of micrometeorites. *Meteoritics Planet. Sci.* **46**, 1498–1509.

Taylor S., Matrajt G. and Guan Y. (2012) Fine-grained precursors dominate the micrometeorite flux. *Meteoritics Planet. Sci.* **47**, 550–564.

Tomeoka K., McSween, Jr, H. Y. and Buseck P. R. (1989) Mineralogical alteration of CM carbonaceous chondrites: a review. *Proc. NIPR Symp. Antarct. Meteorites* **2**, 221–234.

Tomeoka K., Kiriyama K., Nakamura K., Yamahana Y. and Sekine T. (2003) Interplanetary dust from the explosive dispersal of hydrated asteroids by impacts. *Nature* **423**, 60–62.

Tonui E. K., Zolensky M. E., Lipschutz M. E., Wang M. S. and Nakamura T. (2003) Yamato 86029: aqueously altered and thermally metamorphosed CI-like chondrite with unusual textures. *Meteoritics Planet. Sci.* **38**, 269–292.

Tonui E., Zolensky M., Hiroi T., Nakamura T., Lipschutz M. E., Wang M. S. and Okudaira K. (2014) Petrographic, chemical and spectroscopic evidence for thermal metamorphism in carbonaceous chondrites I: CI and CM chondrites. *Geochim. Cosmochim. Acta* **126**, 284–306.

Toppani A., Libourel G., Engrand C. and Maurette M. (2001) Experimental simulation of atmospheric entry of micrometeorites. *Meteoritics Planet. Sci.* **36**, 1377–1396.

Toppani A. and Libourel G. (2003) Factors controlling compositions of cosmic spinels: application to atmospheric entry conditions of meteoritic materials. *Geochim. Cosmochim. Acta* **67**, 4621–4638.

van Ginneken M., Folco L., Cordier C. and Rochette P. (2012) Chondritic micrometeorites from the Transantarctic Mountains. *Meteoritics Planet. Sci.* **47**, 228–247.

van Ginneken M., Genge M. J., Folco L. and Harvey R. P. (2016) The weathering of micrometeorites from the Transantarctic Mountains. *Geochim. Cosmochim. Acta* **179**, 1–31.

Velbel M. A. and Palmer E. E. (2011) Fine-grained serpentine in CM2 carbonaceous chondrites and its implications for the extent of aqueous alteration on the parent body: a review. *Clays Clay Min.* **59**, 416–432.

Vernazza P., Delbo M., King P. L., Izawa M. R. M., Olofsson J., Lamy P., Cipriani F., Binzel R. P., Marchis F., Merín B. and Tamanai A. (2012) High surface porosity as the origin of emissivity features in asteroid spectra. *Icarus* **221**, 1162–1172.

Vokrouhlický D., Nesvorný D. and Bottke W. F. (2008) Evolution of dust trails into bands. *Astrophys. J.* **672**, 696–712.

Wang L., Zhang M., Redfern S. A. and Zhang Z. (2002) Dehydroxylation and transformations of the 2:1 phyllosilicate pyrophyllite at elevated temperatures: an infrared spectroscopic study. *Clays Clay Min.* **50**, 272–283.

Yang B., Jewitt D. and Bus S. J. (2009) Comet 17P/Holmes in outburst: the near infrared spectrum. *Astron. J.* **137**, 4538–4546.

Zhang M., Redfern S. A., Salje E. K., Carpenter M. A. and Wang L. (2010) H2O and the dehydroxylation of phyllosilicates: an infrared spectroscopic study. *Am. Miner.* **95**, 1686–1693.

Zolensky M., Bland P., Brown P. and Halliday I. (2006) Flux of extraterrestrial materials. In *Meteorites and the Early Solar System II* (eds. D. S. Lauretta, H. Y. McSween and A. Z. Tucson). University of Arizona Press, Arizona, pp. 869–888.

Zolensky M., Mikouchi T., Fries M., Bodnar R., Jenniskens P., Yin Q. Z., Hagiya K., Ohsumi K., Komatsu M., Colbert M. and Hanna R. (2014) Mineralogy and petrography of C asteroid regolith: the Sutter's Mill CM meteorite. *Meteoritics Planet. Sci.* **49**, 1997–2016.

Zolensky M., Mikouchi T., Hagiya K., Ohsumi K., Komatsu M., Chan Q.H., Le L., Kring D., Cato M., Fagan A. and Gross J. (2016) Unique view of C asteroids regolith from the Jbilet Winselwan CM chondrite. *Lunar Planet. Sci. XLVI. Lunar Planet. Inst., Houston. #1903(abstr.)*.

Associate editor: Pierre Beck